Exchange of impact-generated dust between the Galilean moons

M.Sc Thesis

Katja Matilainen
Astronomy Research Unit
University of Oulu

April 22, 2020

Contents

1 Introduction **2**

2 Scientific background **3**
2.1 General structure of the jovian dust environment 3
2.1.1 The inner ring system 3
2.1.2 Dust streams originating from Io 3
2.1.3 Dust on the outskirts of the Jupiter system 4
2.2 Dust around the Galilean moons 5
2.2.1 Dust clouds around the moons 5
2.2.2 A tenuous dust ring formed by ejecta from the Galilean moons 5
2.3 Properties, composition and surface chemistry of the Galilean moons 5
2.3.1 Inner structure and composition of Io 6
2.3.2 Inner structure and composition of Europa 7
2.3.3 Inner structure and composition of Ganymede 8
2.3.4 Inner structure and composition of Callisto 8
2.4 Upcoming missions to the Jupiter system 9
2.4.1 Jupiter Icy Moons Explorer (JUICE) 9
2.4.2 Europa Clipper 9

3 Preliminary theoretical considerations, and predictions of the dustmap results **10**
3.1 Representing the eccentricities of dust orbits by a model distribution 11
3.2 Solving for the impact angle of dust crossing the moon orbit 13
3.3 Solving the relative flux of dust on each surface element of the target moon 14
3.4 Coordinate system used in the contour plots 16
3.5 Discussion of results from the model 17
3.5.1 Target moon located interior to the dust ring 17
3.5.2 Target moon outside the dust ring 21
3.5.3 Target moon at the distance of the dust ring 25

4 Comparison to JMEM **27**
4.1 Brief introduction to JMEM 27
4.2 Application of JMEM to evaluate maps of dust fluxes hitting the surfaces of the Galilean moons 29
4.3 Results: Longitude-latitude maps of impact-generated dust fluxes on the Galilean moons 30
4.3.1 Effect of azimuthal position of the moon in the Jupiter system 31
4.3.2 Comparison of fluxes on the surface of different moons . . . 33

4.3.3 Effect of minimum dust particle size 37
4.3.4 Dust from individual source moons 38
4.3.5 Effect of DDS calibration, ejecta distribution exponent, and broken power law 42
4.3.6 Comparison of total fluxes per second on the surface of the Galilean moons 44

5 Discussion and conclusions **45**

1 Introduction

The dust environment of Jupiter consists of various dynamically different parts: tenuous dust rings around the planet, dust streams emanating from the volcanic plumes of Io, impact-generated dust clouds around the Galilean moons, and dilute populations of dust in the outer parts of the Jupiter system [1]. The main source of dust material in the jovian system is impact ejection from the surface of (especially the smaller) moons, caused by high-velocity micrometeoroid impacts. The dust particles are relatively short-lived, and their orbital evolution is influenced by various different forces, including gravitational forces, solar radiation forces, electromagnetic forces and drag due to plasma in the system [1, 2].

Historically, a good majority of research in the Jovian dust environment has focused on the dynamics of the ring system, whereas dust in the vicinity of the Galilean satellites has attracted less attention [2]. However, the measurements in this region by the Galileo dust instrument DDS [3] and the detection of impact-generated clouds [4, 5] have stipulated new interest, especially in view of the forthcoming missions to Jupiter [6, 7].

The goal of this thesis is to derive the fluxes of dust on the surfaces of each of the Galilean moons, using the results on the dust environment of the moons from the Jovian Meteoroid Environment Model (JMEM) [8, 9]. To this end, a program using the software Interactive Data Language (IDL) was created, that directly employs functions from JMEM and then constructs the fluxes on a given surface element of a moon. To visualize the final results, contour plots of the flux distributions on the surface of the four moons were produced, explaining the effect of different parameters for the dust configuration (section 4.3).

To support the interpretation of the final dustmap results in terms of orbital motion and evolution of dust, a simple analytical model using a fixed semimajor axis and a model distribution of eccentricities for the simulated orbits of dust, was used to produce a theoretical distribution of impact angles of dust on the surface of the Galilean moons (see chapter 3).

The following sections 2-4 outline the scientific background for this thesis. This includes an introduction to the dust environment of Jupiter (section 2.1), focusing specifically on the dust around Galilean moons (section 2.2). Some context about the general properties and the composition of the four large moons is also provided in section 2.3. The simple analytical model used as a point of comparison for JMEM results, is described in chapter 3. The Jovian Meteoroid Environment Model and its use in this thesis work is described in section 4. Section 4.3 contains the results from JMEM in form of longitude-latitude maps of the dust fluxes on the surface of the moons. Section 5 provides a discussion and conclusions.

2 Scientific background

2.1 General structure of the jovian dust environment

2.1.1 The inner ring system

The jovian ring system is an archetype of tenuous dust rings. Since its discovery in 1979 by the Voyager I mission [10], the inner ring system has been observed both by visiting spacecraft [11, 12, 13] and from the Earth during Jupiter's ring-plane crossings [14, 15, 16]. By definition, dust rings are faint and sparse, implying that mutual collisions of ring particles are rare [1, 17]. With the exception of some centimeter-sized or larger bodies in the main ring [18], the jovian rings are dominated in number by micron-sized grains [19, 20] that are easily destroyed by various processes in the harsh plasma environment [21]. Thus, the ring material must be constantly replenished by their source moons in order to be a long-lasting feature in the solar system [1, 17].

The structure of the inner ring system can be divided into three distinct components: a vertically narrow *main ring* that transitions into a thick, toroid-shaped *halo* at its inner boundary [22, 23, 24, 25], and the faint, nested set of the two *gossamer rings* [26, 27, 28], that lie radially outside of the inner rings (see figure 1). Each of the rings are tightly linked with one or several small ring-moons, which strongly affect the shape of the rings and probably act as major sources and sinks of dust material for them [23, 24].

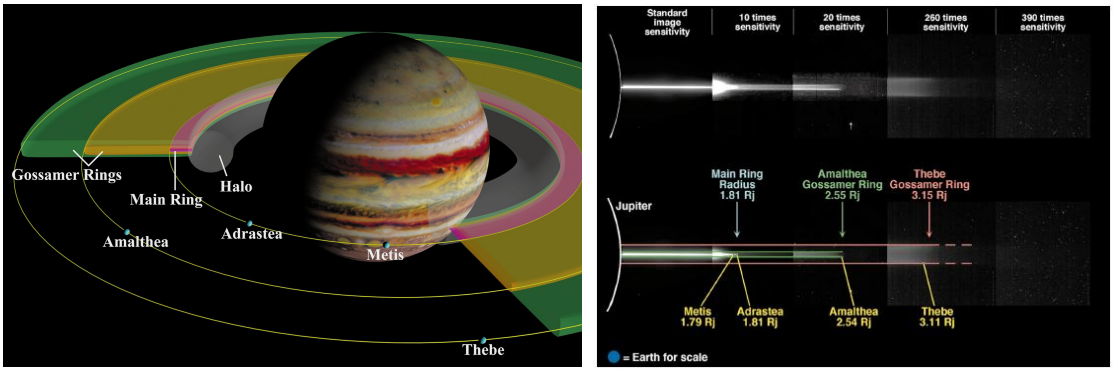

Figure 1: Schematic view (left), and cross-cut (right) of the inner ring system of Jupiter. Graphics taken from [23].

2.1.2 Dust streams originating from Io

The dust streams emanating from the Jupiter system were first detected at large distance in interplanetary space by the Ulysses spacecraft [29, 30, 31, 32, 33, 11],

and later confirmed by the Galileo mission [34, 35, 36]. As those spacecraft traversed interplanetary space, they detected the streams as a signal in their onboard dust counters with a period of 28 days, which arises as a modulation from the variable solar magnetic field [1].

The dust streams most likely originate from the most energetic volcanic plumes on the active moon Io, in which the particles reach high altitudes where they become negatively charged by the ionospheric plasma of Io [37, 1]. The smallest plume particles are then affected by the corotational electric field of Jupiter, which transports the dust away from Io [37]. The particles are eventually re-charged positively in the Jovian magnetosphere and ejected from the Jovian system by the electromagnetic force [38].

2.1.3 Dust on the outskirts of the Jupiter system

The outer region of the Jupiter system, between $50 - 300 R_J$ distance from the planet, is host of small populations of micron-sized dust. The absolute number density level of dust particles in the outskirts of the system is only one order of magnitude higher than the interplanetary background, and the radial number density profile of the dust is remarkably flat throughout the radial distance of $50 - 300 R_J$ [39].

The dust material in the outer jovian region is ejected from the surface of the outer irregular satellites by micrometeoroid impacts. The detached grains have moderate eccentricities, and a wide range of inclinations from prograde to retrograde orbits, following the orbits of their source bodies closely [39]. These tiny source moons can be described as "the Oort cloud of Jupiter". The amount of detected irregular satellites around the giant planets has been skyrocketing in the past few years. Currently there are 61 known irregular satellites around Jupiter [40], most of which orbit the planet in retrograde orbits [41]. Both their orbital and spectral properties strongly resemble dormant Oort cloud comets, and it is likely that the irregular satellites were captured from their initially heliocentric orbits during violent reshuffling events in the solar system [41, 39, 42, 43].

Recent numerical modelling suggests that a portion of the dark debris from irregular satellites is driven towards Jupiter by Poynting-Robertson drag, and ends up in the surface of Galilean moons. It is even possible that this flux of material has been a significant source of organic material to Europa's subsurface ocean [42].

2.2 Dust around the Galilean moons

2.2.1 Dust clouds around the moons

The in situ dust detector onboard Galileo detected faint dust clouds surrounding the Galilean moons [4, 44, 45, 46]. The clouds are most likely of impact-generated origin, and they share very similar physical properties [45]. The size distribution of particles in the clouds is comparable for all the moons, with decreasing numbers towards bigger particles, although the slightly less steep slope for Europa may indicate that its surface material may be more loose than on the other satellites. The radial density profiles for the clouds are also very much alike, and their concentration towards the moon's surface is consistent with predictions by dynamic models for their impact-generated origin [47]. The density profiles are in agreement with model predictions for ice-silicate surfaces, although the noticeably lower density near Io suggests that its surface may be softer and "fluffier" compared to the other moons, due to deposits of sulfur-rich volcanic material on its surface [45].

The clouds seem to have a leading-trailing asymmetry: the number density is slightly higher in the leading side of the moon, due to the higher flux and larger impact speeds of the impacting micrometeoroids on the leading side [48, 49].

2.2.2 A tenuous dust ring formed by ejecta from the Galilean moons

The existence of a dust ring in the region of the Galilean moons has been indicated since the few early dust grain detections by Pioneer 10/11 [50, 51] and Ulysses spacecraft [1], and later confirmed by further *in situ* measurements by the Galileo dust detector [52].

The Galilean ring consists of dust material ejected from the surface of Galilean moons by micrometeoroid impacts [2, 53]. In contrast to the dust detached from the small moons in the inner Jupiter system, most of the material ejected from the Galilean moons moves on ballistic trajectories and re-impacts the surface of the moons [52, 5]. Only a small fraction of the ejected dust manages to escape into circumjovian orbits, forming a broad, but extremely faint ring concentrated slightly outside the orbit of Europa [53, 52]. The number density of the ring is around 500km^{-3} near Europa's orbit [52, 3], about two orders of magnitude lower than in the faint gossamer rings [28], making the Galilean ring far too tenuous for optical detection.

2.3 Properties, composition and surface chemistry of the Galilean moons

The four large Galilean satellites can be thought of as a "miniature solar system" orbiting around Jupiter, in a sense that they all are roughly similar in size, they

have prograde, coplanar orbits, and their composition consists of a mixture of metal, rock and ice. The exact amounts of the three components, and the degree of differentiation between the materials depend on the moon's distance from Jupiter: as the distance from the planet increases, the degree of differentiation goes down, and the amount of ice material included in the mixture increases [54].

The exact inner structure of the Galilean moons is still unknown, but there are several constraints on the possible two- or three-layer models for the moons, collected from the measured higher order gravity coefficients [55, 56, 57, 58, 59, 60, 61, 62], from magnetic field data for the moons [63, 64, 65, 66, 67, 68, 69], and from imaging and infrared observations. A sketch of the probable inner structure of the moons is found in figure 2.

Spectroscopic data of the surfaces of the Galilean moons show that ice is the major component on the surfaces of Europa, Ganymede, and Callisto, and the densities suggest that the latter two contain rock/iron and ice in approximately equal shares [54]. Io is composed of mostly rock and iron with water completely absent from the surface. Instead, sulfur and sulfur dioxide are widespread on its surface [70].

The moons have a variety of both endogenic and exogenic resurfacing processes acting on their surface. The crust of the innermost Galilean satellite Io is in a state of constant, global renewal through the volcanic activity powered by its intense tidal heating [70, 71].

2.3.1 Inner structure and composition of Io

The innermost Galilean satellite Io is the most differentiated of the four moons, and the only one with no ice layer at all [72]. The strong tidal forces of Jupiter cause intense flexing and heating of the moon's mantle [73, 74, 75], and act as a driving force behind Io's intense volcanic activity [76, 77]. The bulk composition of Io is estimated to be close to that of the L and LL chondrites, consisting mostly of olivine [78]. The upper mantle of the moon is at least partially molten, and covered by a thin, low-density crust of mafic material, differentiated by the moon's volcanic activity [79].

Precise measurements of Io's gravity field strongly suggest that Io is in hydrostatic equilibrium, and models of the moon's interior density imply that it has a metallic core of either pure iron or iron sulfide (Fe or FeS) [55, 79]. The core size ranges somewhere between $38 - 53\%$ of the satellite's radius, depending on the amount of lighter components like sulfur in its composition [54]. Despite initial evidence of a possible intrisic magnetic field of Io [63], further polar passes of the moon by the Galileo orbiter made it clear that an internal magnetic field is negligibly small and probably absent, ruling out the possibility of a convecting core with dynamo action [80, 81, 82].

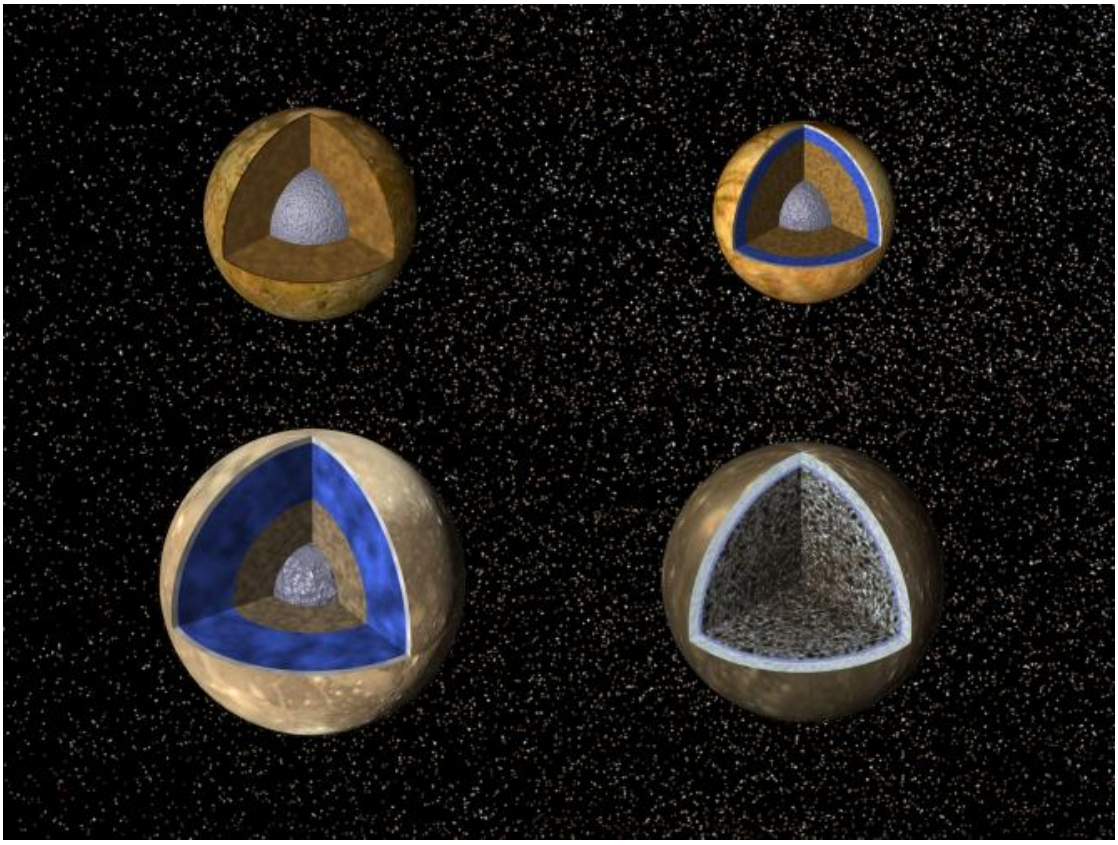

Figure 2: Sketch of the probable inner structure of the Galilean moons Io (upper left), Europa (upper right), Ganymede (lower left) and Callisto (lower right). Graphic taken from JPL release PIA01082.

2.3.2 Inner structure and composition of Europa

Europa is a rocky, ice-covered object slightly smaller than the Earth's moon [83]. Its low moment of inertia suggests that the moon is differentiated into a metallic core surrounded by a rocky mantle and a water ice-liquid shell [57, 60]. In the potential three-layer models for Europa, the mantle density is consistent with an olivine-dominated mineralogy, similar to Io [54].

Depending on the exact composition of the core (Fe or FeS), its estimated core sizes range somewhere between $13 - 45\%$ of the moon's radius [60, 54]. Both the estimated core size and mantle density of Europa depend substantially on the thickness of its ice layer, which varies somewhere between 80-170km [60, 54].

Based only on the gravitational data from the Galileo flybys [57, 60], the composition of the outer ice shell could be either partially melted or completely solid, as it makes no difference in the measured moment of inertia. However, the Galileo

magnetometer measurements revealed that Europa must have an electrolyte-rich ocean under its surface layer of ice [84]. The moon has an induced, varying dipole field that matches the synodic period of Jupiter and the orientation of the planet's magnetic field [85, 69]. The conducting layer responsible for the induced field must be located less than 200km deep from the surface, and its conductive properties match a salt-water ocean at least a few kilometers deep [86].

2.3.3 Inner structure and composition of Ganymede

Ganymede is the largest satellite in the solar system, with highly planet-like evolution and physical properties [87]. The bulk composition of Ganymede is almost equal parts rock (60%) and ice (40%), and gravity data from the Galileo encounters implies that the moon is highly differentiated, with an iron core and a silicate mantle, covered by a thick ($\sim$ 800km) ice layer [55].

In the different interior models calculated for the moon, a pure olivine mantle seems to be a reasonable approximation [54, 75], but models based on carbonaceous chondrite-like mantle composition exist as well [88]. Refining the compositional model would require a more detailed analysis of the gravitational field of Ganymede.

The size of the moon's core should be somewhere between $25-33\%$ of its radius, depending on how sulfur-rich its composition is [54]. Detection of an intrinsic magnetic dipole field of Ganymede suggests that the core either supports current dynamo action, or its previous magnetic activity has magnetised the ferromagnetic rock core, causing a remanent magnetic field [89, 66, 65].

In addition to the intrinsic dipole field, the magnetic field of Ganymede has an induced component, suggesting that the moon has a conductive shell somewhere in the first few hundred kilometers beneath its surface [90]. The most probable explanation is a few tens of kilometers thick liquid salt-water ocean, located between layers of ice [90]. The existence of a liquid water layer implies that the thermal gradient of the ice layer is steep, and its internal structure can be subdivided into pressure-induced ice I, ice III, ice V, and ice VI phases [54].

2.3.4 Inner structure and composition of Callisto

Callisto is very similar to Ganymede in size and composition, consisting of similar fractions of ice (40%) and rock-iron (60%) [58]. The relatively high moment of inertia measured by Galileo [58, 59, 60, 62], as well as the apparent lack of an intrinsic magnetic field [91], indicate that unlike its slightly larger neighbour, Callisto seems to be only partially differentiated. The critical difference in the degree of differentiation between the two moons may be a consequence of past tidal heating of Ganymede, related to its Laplace resonance with Io and Europa [87].

The interior structure of Callisto is even less well constrained than that of the other galilean moons. It is possible that Callisto is differentiated into three layers: a rock-metal core, a middle layer consisting of a mixture of rock and ice, and an outer layer of water-ice. However, two-layer models where under a thin (< 300km) layer of clean ice, rock-metal and ice components are mixed all the way to the center of the moon, cannot be excluded either [60, 62, 54].

Like the other ice-rich galilean moons (Europa and Ganymede), Callisto has an induced magnetic field that requires the existence of a conducting layer less than a few hundred kilometers below its surface, indicated by the magnetic field data from the Galileo mission. The conductivity of this layer calls for a subsurface ocean, or at the very least, a partially molten layer of ice [86, 84].

2.4 Upcoming missions to the Jupiter system

2.4.1 Jupiter Icy Moons Explorer (JUICE)

The Jupiter icy moons explorer (JUICE) is the first large-class mission in the Cosmic Vision 2015-2025 programme of European Space Agency (ESA) (`https://sci.esa.int/web/juice/home`) [92]. The major science themes for JUICE are to study the Jupiter system as an archetype for gas giants, and to investigate the emergence of habitable worlds around giant planets, focusing especially on the largest Galilean moon Ganymede. Key objectives for this mission include determinining the composition and distribution of surface materials, especially related to habitability, and characterizing the extent of oceans under the icy shells of the moons Europa, Ganymede and Callisto. [93, 7, 6]

Scheduled for launch in 2022 and arrival at Jupiter in 2029, JUICE will complete two close passes over Europa and multiple flybys of Ganymede and Callisto before settling in its orbit around Ganymede. The spacecraft is currently planned to impact the surface of Ganymede at the end of the mission in 2033, after approximately three years of touring the Jupiter system [94, 93]. The JUICE model payload consists of 10 instruments, dedicated for both remote sensing (imaging, radar) and for performing in situ measurements (e.g. magnetometer, plasma and radio wave sensors) [92, 93].

2.4.2 Europa Clipper

The Europa Clipper spacecraft (`https://www.jpl.nasa.gov/missions/europa-clipper/`) is planned to launch in the 2020s by the National Aeronautics and Space Administration (NASA). The spacecraft will orbit around Jupiter and perform 45 close passes over Europa, shifting its flight path for each flyby in such a manner that it will eventually scan nearly the entire surface area of the moon. [95]

The main science goal for the mission is to explore the habitability of the moon, by studying its ice shell and ocean, composition and geology [96]. This will especially include investigating the chemistry and origin of the non-ice components in the surface, as well as exchange processes between the interior and the surface of the moon. An important secondary goal for the mission is to scout for scientifically promising sites for future mission landings.

Europa Clipper's payload will include cameras and spectrometers to produce high-resolution images and compositional maps of Europa's surface and thin atmosphere, an ice-penetrating radar to search for subsurface water, and magnetometer and gravity measurements to measure the moon's magnetic field and unlock clues about its ocean and deep interior [97, 96].

From the perspective of dust research, an instrument of special interest onboard the Europa Clipper is the SUrface Dust Analyzer (SUDA), which will detect and analyze dust particles ejected from the surface of Europa by high-velocity micrometeoroid impacts. In this way, SUDA will provide direct measurements of the composition of samples from the surface. [95]

If the existence of water plumes, previously predicted as a part of cryovolcanic activity on the moon [71, 98, 99, 100] and further hinted at by the detection of water vapor by NASA's Hubble Space Telescope [101, 102, 103, 104] is confirmed by the spacecraft and linked to a subsurface ocean, studying the composition of particles entrained in the plume with SUDA will provide information about the chemical makeup of Europa's interior, potentially habitable environment without having to drill through layers of ice [105].

3 Preliminary theoretical considerations, and predictions of the dustmap results

In this section a rough theoretical estimate is developed for distribution of the dust flux on the surface of a moon. In this model, the orbits of the moons are simplified as circular Keplerian orbits with no eccentricity or inclination, the semimajor axis a_{dust} of all dust particles is kept constant, and only the eccentricity of dust orbit is treated as a distributed number.

Ignoring all other variables except eccentricity ϵ gives a reasonable first-order approximation for the expected locations of minimum and maximum values of the number flux of dust impacting on the surface of the moon. Including distributed values for inclination i_{dust} and semimajor axis a_{dust} of the dust would add complexity to the model without changing the essential outcome of the program much.

The value $a_{\text{dust}} = 14.978002 R_J$, the semimajor axis of Ganymede, is chosen as

the semimajor axis of all simulated dust orbits. This is roughly equivalent to a situation where the dust particles are originated from Ganymede. The reasoning behind choosing Ganymede as the source moon in our example case is, that it provides the most well-behaved comparison with the results from JMEM. The dynamics of particles from the inner Galilean moons (Io and Europa), especially for smaller particle sizes ($< 10\mu m$), are more affected by non-gravitational forces, so their behaviour is less comparable to the basic Keplerian principle behind leading-trailing anomalies on the surface of the moons.

Three different prototype cases for relative locations of dust source and the target moon are considered in the simple model: target moon inside the dust ring ($a_{\mathrm{moon}} < a_{\mathrm{dust}}$), target moon outside the dust ring ($a_{\mathrm{moon}} > a_{\mathrm{dust}}$), and target moon inside the dust ring ($a_{\mathrm{moon}} = a_{\mathrm{dust}}$). The case $a_{\mathrm{moon}} < a_{\mathrm{dust}}$ corresponds to dust transfer from source Ganymede to the surface of Io and Europa (see discussion in chapter 3.5.1), case $a_{\mathrm{moon}} > a_{\mathrm{dust}}$ corresponds to dust transfer from source moon Ganymede to the surface of Callisto (section 3.5.2), and finally the case $a_{\mathrm{moon}} = a_{\mathrm{dust}}$ corresponds to dust from source moon Ganymede re-impacting on the surface of Ganymede.

3.1 Representing the eccentricities of dust orbits by a model distribution

For satellites on circular orbits the distance from the central object is constant (1).

$$r_{\mathrm{moon}} = a_{\mathrm{moon}} \tag{1}$$

In our example the moon Ganymede is picked as the initial source of dust particles, and its semimajor axis is used as the semimajor axis of all the generated orbits of dust ($a_{\mathrm{dust}} = a_{\mathrm{Ga}}$). For simplicity, inclination of the dust orbits is kept as a constant $i = 0$ (co-planar with Jupiter's equatorial plane) as well, and only the possible eccentricity values of dust orbits are varied. Still, the dust is considered as a stream that has some vertical extension larger than the moon diameter, so that the stream particles hit all latitudes of the target moon. The orbits of dust follow Kepler's first law

$$r_{\mathrm{dust}}(f) = \frac{a_{\mathrm{dust}}(1 - \epsilon_{\mathrm{dust}}^2)}{1 + \epsilon_{\mathrm{dust}} \cos f}\,, \tag{2}$$

where ϵ_{dust} is the eccentricity of the orbit, a_{dust} is the semimajor axis of the orbit, and f is the true anomaly measured counterclockwise from the pericenter of the orbit.

For impact to be possible, the orbits of dust and the target moon need to cross. If the semimajor axis of the particle and the target moon are different, this

is only possible when the eccentricity of the dust orbit exceeds a certain minimum eccentricity $\epsilon_{\min}$, depending on the $\frac{a_{\text{moon}}}{a_{\text{dust}}}$ ratio.

If the semimajor axis of the target moon is larger than the semimajor axis of dust, the condition for crossing is, that the apocenter distance $r_{\text{dust,max}}$ (largest possible distance from Jupiter) of dust must be larger than a_{moon}:

$$r_{\text{dust,max}} > a_{\text{moon}} \tag{3}$$
$$a_{\text{dust}}(1+\epsilon) > a_{\text{moon}} \tag{4}$$
$$\rightarrow \quad \epsilon > \frac{a_{\text{moon}}}{a_{\text{dust}}} - 1\,. \tag{5}$$

Similarly, if $a_{\text{moon}} < a_{\text{dust}}$, the pericenter distance $r_{\text{dust,min}}$ (smallest possible distance from Jupiter) of dust must be smaller than a_{moon}:

$$r_{\text{dust,min}} < a_{\text{moon}} \tag{6}$$
$$a_{\text{dust}}(1-\epsilon) < a_{\text{moon}} \tag{7}$$
$$\rightarrow \quad \epsilon > 1 - \frac{a_{\text{moon}}}{a_{\text{dust}}}\,. \tag{8}$$

From equations (5) and (8) we get the minimum required eccentricity

$$\epsilon_{\min} = \left| 1 - \frac{a_{\text{moon}}}{a_{\text{dust}}} \right|\,. \tag{9}$$

To create a randomized distribution of eccentricities for the simulated dust grain orbits, a Rayleigh distribution is applied

$$f(\epsilon;\sigma) = c\frac{\epsilon}{\sigma^2} e^{-\frac{\epsilon^2}{2\sigma^2}}\,, \quad \epsilon \geq \epsilon_{\min} \tag{10}$$

The normalization constant c is fixed by using the previously solved $\epsilon_{\min}$, and setting the total probability of all possible eccentricity values to 1. The maximum value of eccentricity is set to $\epsilon_{\max} = 1$, so that only bound orbits are taken into account. Here σ determines the width of the distribution. It is set to the value $\sigma = 0.2$, producing a fairly narrow distribution.

$$\int_{\epsilon_{\min}}^{1} f(\epsilon) d\epsilon = 1 \tag{11}$$
$$\rightarrow c = -\frac{1}{\left(e^{-\frac{\epsilon_{\max}^2}{2\sigma^2}} - e^{-\frac{\epsilon_{\min}^2}{2\sigma^2}} \right)}\,. \tag{12}$$

To be able to create random deviates for the Rayleigh distribution numerically with IDL in a simple manner, an exchange of variables from a uniform probability distribution of x values between $[0, 1]$ to a Rayleigh distribution of eccentricity values between $[\epsilon_{\min}, 1]$ has to be made. This can be done by setting

$$f(\epsilon)d\epsilon = p(x)dx\,, \tag{13}$$

where $p(x) = 1$ everywhere for a uniform probability distribution. This leads to

$$\int dx = \int f(\epsilon)d\epsilon \tag{14}$$

$$\rightarrow x + k = -ce^{-\frac{\epsilon^2}{2\sigma^2}} \tag{15}$$

$$\rightarrow \epsilon = \underline{\underline{\sqrt{-2\sigma^2 \log\left(-\frac{1}{c}(x+k)\right)}}}\,,\ 0 \leq x \leq 1\,. \tag{16}$$

The constant k can be solved from equation 15 by setting $x = 1$ for $\epsilon = 1$. Now Rayleigh distributed deviates ϵ can be generated with IDL by taking n values of uniformly randomized randomu(x), and solving the corresponding ϵ values from 16. An example of the distribution presented in a histogram form, is shown in figure 15 (see also figures 7 and 11).

3.2 Solving for the impact angle of dust crossing the moon orbit

In the planar configuration the orbits of dust have two possible values of the true anomaly f_1 and f_2 where collision with the target moon can happen (see fig 7). These two locations can be obtained by setting

$$r_{\text{moon}} = r_{\text{dust}}(f) \tag{17}$$

$$\rightarrow \quad a_{\text{moon}} = \frac{a_{\text{dust}}(1-\epsilon_{\text{dust}}^2)}{1+\epsilon_{\text{dust}}\cos f} \tag{18}$$

$$\rightarrow \quad \cos f = \frac{1}{\epsilon_{\text{dust}}}\left(\frac{a_{\text{dust}}}{a_{\text{moon}}}(1-\epsilon_{\text{dust}}^2) - 1\right) \tag{19}$$

$$\rightarrow \quad f_{1/2} = \pm \arccos\left(\frac{1}{\epsilon_{\text{dust}}}\left(\frac{a_{\text{dust}}}{a_{\text{moon}}}(1-\epsilon_{\text{dust}}^2) - 1\right)\right)\,. \tag{20}$$

To obtain the impact angles of dust on the surface of the target moon, we need to know the velocity vectors of dust and the target moon at the two locations in their orbit (f_1 and f_2) where collisions can happen. The orbital velocity vector of

a dust particle on an elliptic orbit is

$$\bar{v}_{\mathrm{dust}} = \sqrt{\frac{\mu}{a_{\mathrm{dust}}(1-\epsilon^2)}}\epsilon \sin f \hat{u}_r + \sqrt{\frac{\mu}{a_{\mathrm{dust}}(1-\epsilon^2)}}(1+\epsilon\cos f)\hat{u}_\phi \,, \qquad (21)$$

where $\mu \approx GM_{\mathrm{Jupiter}}$ is the universal gravitational constant G multiplied by the mass of the planet M_{Jupiter}, $\hat{u}_r$ is a unit vector pointing radially outwards from the planet, and $\hat{u}_\phi$ is a unit vector pointing in the azimuthal direction (direction of the local Kepler velocity), perpendicular to the radial direction. The orbital velocity of a moon on a circular orbit is the local Kepler velocity

$$\bar{v}_{\mathrm{Kepler}} = \sqrt{\frac{\mu}{a_{\mathrm{moon}}}}\hat{u}_\phi \,. \qquad (22)$$

The angle α between the direction of the motion of the moon $\bar{v}_{\mathrm{Kepler}}$ and the direction of the dust motion $\bar{v}_{\mathrm{rel,dust}} = \bar{v}_{\mathrm{dust}} - \bar{v}_{\mathrm{Kepler}}$ can be solved from the dot product of the two vectors:

$$\cos\alpha = \frac{\bar{v}_{\mathrm{Kepler}} \cdot \bar{v}_{\mathrm{rel,dust}}}{|\bar{v}_{\mathrm{Kepler}}||\bar{v}_{\mathrm{rel,dust}}|} \,. \qquad (23)$$

Using the distribution of eccentricities given by equation (10), the number of impacting grains from each direction α is solved and stored as a histogram (see figures 7, 11 and 15). The angle α is measured from the apex direction of the moon, and by definition shows the direction where the dust particle is *going to* (angle α between $\bar{v}_{\mathrm{Kepler}}$ and $\bar{v}_{\mathrm{rel,dust}}$), and not the direction the impacting dust particles are *coming from* (angle $\alpha + 180°$, between $\bar{v}_{\mathrm{Kepler}}$ and $-\bar{v}_{\mathrm{rel,dust}}$). To facilitate comparison with the final contour plots, the α-histogram results are presented using the angle $\alpha + 180°$.

3.3 Solving the relative flux of dust on each surface element of the target moon

The flux of dust on the surface of the target moon varies according to the relative orientation of a surface element of the moon, compared to the direction of velocity of the incoming stream of dust. To be able to produce longitude-latitude plots of the simulated dust number density, the surface of the moon needs to be divided into a grid of surface elements (see figure 3), and the number flux of impacting dust particles must be evaluated individually for each element.

The orientation of each surface element is specified by a normal unit vector $\hat{k}_{\theta,\phi}$ located at the center of the element, pointing radially outwards from the center of the moon. The vector $\hat{k}_{\phi,\theta}$ consists of two angular components, k_θ and k_ϕ.

The angle k_θ is measured from the north pole of the moon, and the angle k_ϕ is measured clockwise from the apex direction. In the simple model the surface of the target moon is divided into a grid of 36×18 elements: 36 equidistant k_ϕ values between $0° \leq k_\phi \leq 360°$, and 18 equidistant k_θ values between $0° \leq k_\theta \leq 180°$ are used to represent the surface of the moon ($10°$ difference between neighbouring $\hat{k}_{\phi,\theta}$-vectors).

From the orientation of the surface element, and the direction of velocity of the approaching stream of dust, we get three coefficients C_{lat}, C_{long} and Θ that affect the number of impacting dust particles. The functions

$$C_{lat}(k_\theta) = |\sin(k_\theta)|$$

and

$$C_{long}(k_\phi, \alpha) = \cos|(\alpha + 180°) - k_\phi|$$

are cosine terms that take into account the effect of reduced crosscut area for a dust stream approaching a tilted surface (non-perpendicular to the direction of the relative velocity of the dust). The coefficient

$$\Theta(k_\theta, k_\phi, \alpha) = \begin{cases} 1, & C_{\text{long}} > 0 \\ 0, & C_{\text{long}} < 0 \end{cases} \tag{24}$$

is the heaviside function, which makes sure that we only take into account dust particles that are approaching the surface of the target moon from outside of the moon.

The total sum of impacting particles $N(k_\phi, k_\theta)$ is calculated individually for each surface element. Each bin n_α (relative number of particles approaching the target moon from direction α) of the impact angle histogram (see figures 7, 11 and 15) is multiplied by the corresponding $\Theta(k_\theta, k_\phi, \alpha)$, $C_{lat}(k_\theta)$ and $C_{long}(k_\phi, \alpha)$ coefficients, and the total number of impacting particles $N(k_\phi, k_\theta)$ is summed together for the surface element in question.

$$N(k_\phi, k_\theta) = \sum_\alpha \Theta(k_\theta, k_\phi, \alpha) C_{lat}(k_\theta) C_{long}(k_\phi, \alpha) n_\alpha \tag{25}$$

The final results are then presented as contour plots showing the relative flux on each surface element (see figures 8, 12 and 16 for the results from the simple model, and chapter 4 for results from the JMEM-dependent program).

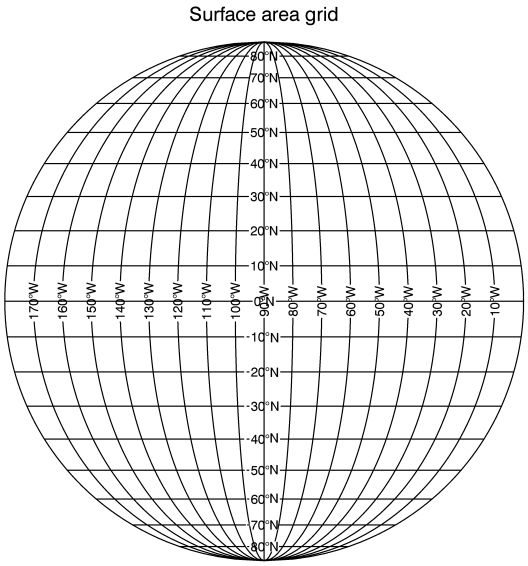

Figure 3: Longitude-latitude grid of the leading side of the target moon. W = western longitude, N = northern latitude. Graphic created with IDL.

3.4 Coordinate system used in the contour plots

Due to tidal locking, all of the four Galilean moons are in a state of bound rotation around Jupiter, i.e. their orbital period around the planet and the period of rotation around their axis are exactly the same. This spin-orbit coupling means that the same side of the moon is always facing towards the planet, which provides a fixed zero-point for a moon-centric longitude-latitude angle coordinate system for mapping the surface of the moons. For simplicity, the effect of libration caused by the small but non-vanishing eccentricities of the moons is ignored in the dustmaps.

In all the dust density flux contour plots shown in sections 3.5 and 4.3, the longitude angle of each surface element on the moon is measured clockwise (western longitude, WL) from the Jupiter direction (WL = 0°). In this fixed, non-inertial frame, the direction of the moon's velocity (local Kepler velocity) is constant, pointing in the WL = 90° direction. The longitude WL = 180° corresponds to the anti-jovian direction, while WL = 270° points "backwards" in the direction opposite to the moon's velocity. The longitude values between 0° < WL < 180° are referred to as the "leading side" of the moon, as they face the direction of its orbital velocity. Similarly, the longitude values between 180° < WL < 360° make up the "trailing side" of the moon. The latitude angle is measured from the equatorial plane (northern latitude, NL) of the moon in question (NL = 0° at the

equator), so that NL = +90° at the geographical "north pole" of the moon, and NL = −90° at its "south pole". A visualization of the longitude-latitude grid used in contour plot creation is presented in figure 3 in chapter 3.3.

3.5 Discussion of results from the model

The final results for the three prototype cases are presented as longitude-latitude contour plots, similar to the results of the main JMEM-dependent program in section 4. Some background and analysis of the expected behaviour is provided through histogram plots of relative dust velocities and impact angles, as well as example plots of the crossing orbits of dust and the target moon.

3.5.1 Target moon located interior to the dust ring

For a target moon located interior to the dust source ($a_{\text{moon}} < a_{\text{dust}}$), the majority of the flux is expected on the trailing side of the moon. In this situation, on average, the dust grains cross the orbit of the target moon when they are close to the pericenter r_{min} of their orbit (see figures 4 and 6), where their tangential velocity is higher than the local Kepler velocity (see figure 4 and equations 26-29). Since the tangential velocity of dust is larger than the tangential velocity of the target moon, the particles impact the surface of the moon "from the back".

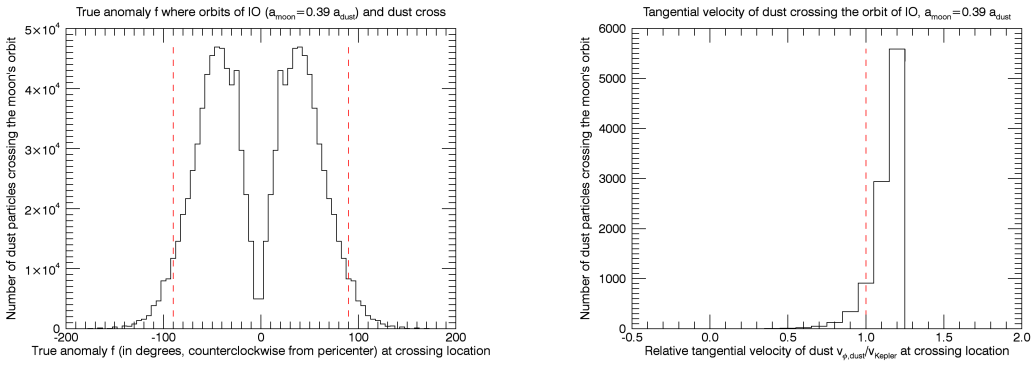

Figure 4: Histograms of the true anomaly f (left), and the relative tangential velocity of dust grains (right) at the crossing location for the case $a_{\text{moon}} < a_{\text{dust}}$. The majority of dust particles originated from a dust ring outside the orbit of the target moon cross the orbit of the moon near the pericenter of their orbit ($-90° < f < 90°$, marked with the red dotted lines in the figure at left), where their tangential velocity is larger than the local Kepler velocity ($v_{\phi,\text{dust}}/v_{\text{Kepler}} > 1$).

The tangential velocity of a dust grain in an elliptic orbit is (tangential part of

$\bar{v}_{\mathrm{dust}}$ presented in equation 21):

$$v_{\mathrm{dust},\phi} = \sqrt{\frac{\mu}{a_{\mathrm{dust}}(1-\epsilon^2)}}(1+\epsilon\cos f)\,, \tag{26}$$

which can be presented using the distance $r_{\mathrm{dust}}(f)$ from Jupiter (Kepler's first law, equation 2) as

$$v_{\mathrm{dust},\phi} = \sqrt{\frac{\mu}{r_{\mathrm{dust}}(f)}}\sqrt{1+\epsilon\cos f}\,. \tag{27}$$

At the locations where the orbits of dust and the target moon cross, distance from the planet is $r_{\mathrm{dust}} = a_{\mathrm{moon}}$, and the local Kepler velocity is $v_{\mathrm{Kepler}} = \sqrt{\mu/a_{\mathrm{moon}}}$, so

$$v_{\mathrm{dust},\phi} = v_{\mathrm{Kepler}}\sqrt{1+\epsilon\cos f}\,. \tag{28}$$

Since $\epsilon > 0$ for all particles crossing the moon's orbit, we get that

$$v_{\mathrm{dust},\phi} > v_{\mathrm{Kepler}} \quad \text{when} \quad \cos f > 0\,. \tag{29}$$

As figure 4 shows, for our chosen distribution of eccentricities (see figure 7), the majority of impacts happens near the pericenter of the dust orbits where $\cos f > 0$ ($-90° < f < 90°$). Only the particles on highly eccentric orbits ($\epsilon > 0.8$) cross the orbit of the target moon further away from the pericenter, where their tangential velocity is less than the local Kepler velocity (see figure 5).

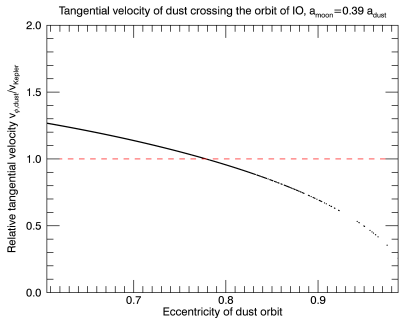

Figure 5: Relative tangential velocity of dust at the locations where orbits of target moon and dust grain cross (local Kepler velocity signified by the red dashed line). Dust grains with larger eccentricities ($\epsilon > 0.8$) cross the orbit of the moon further away from the pericenter, where their tangential velocity is lower than the local Kepler velocity.

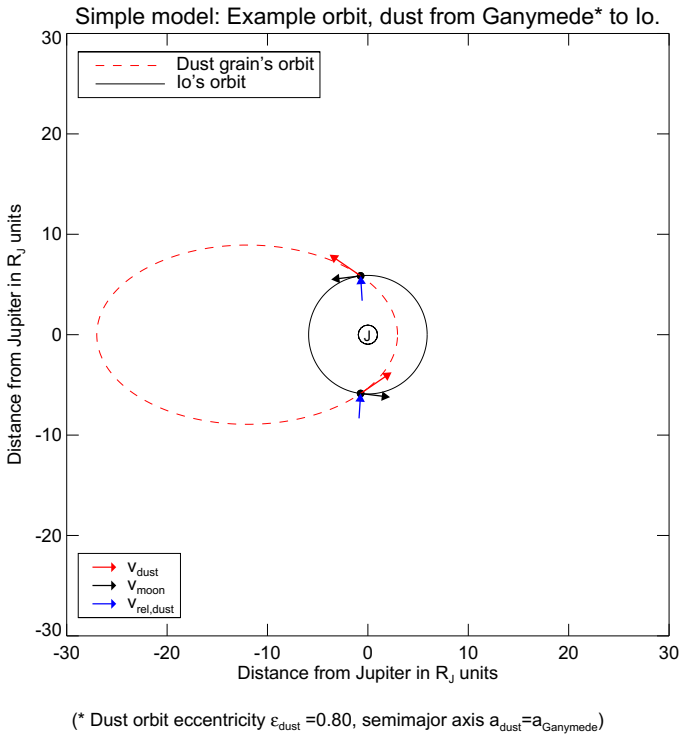

Figure 6: Example plot of the intersecting orbits of the moon Io, and a dust grain from Ganymede's distance.

The relation $v_{\mathrm{dust},\phi}/v_{\mathrm{Kepler}}$ only tells if the impact happens on the leading or trailing hemisphere of the moon. The relative radial velocity of dust is also required to determine the impact angles of dust. If the radial component of $\bar{v}_{\mathrm{dust,rel}}$ is large compared to its tangential component at the locations where the orbits cross, the dust approaches the surface of the moon near the Jupiter and anti-Jupiter directions. If the radial component is insignificant compared to the tangential velocity, the maximum of dust flux should be close to the apex or anti-apex directions.

As the Galilean moons are on near-circular orbits ($\epsilon \approx 0$), they have no radial velocity, and the relative radial velocity of dust crossing the orbit of the target moon is simply the radial component of the dust particle's velocity:

$$v_{\mathrm{dust},r} = \sqrt{\frac{\mu}{a_{\mathrm{dust}}(1-\epsilon^2)}}\epsilon \sin f \tag{30}$$

From equation (30) and the plot of example orbits in figure 6 it is seen, that the radial velocity $v_{\mathrm{dust},r}$ has equal, but opposite values at the two crossing locations f_1 and $f_2 = -f_1$. This property is reflected in the impact angle histogram in figure

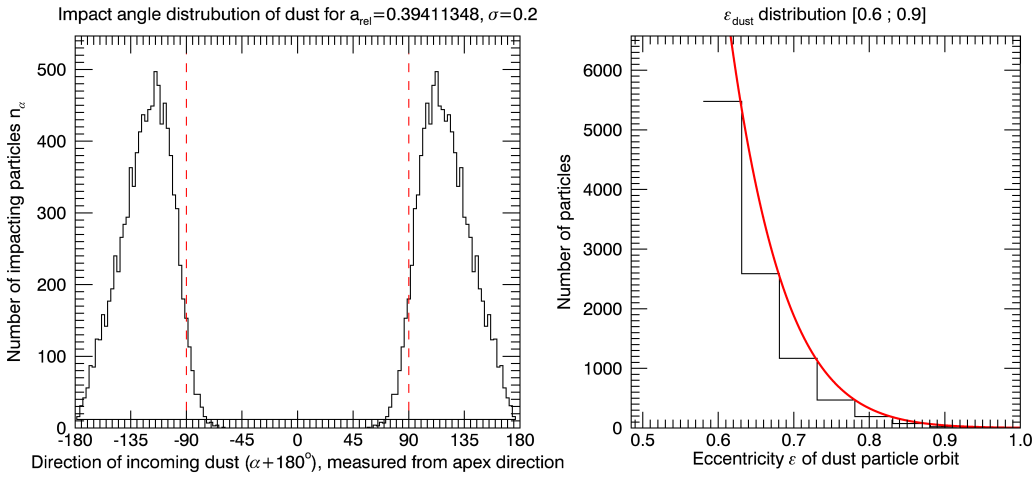

Figure 7: Model distribution of impact angles for dust from Ganymede impacting the surface of Io (left), and the corresponding Rayleigh distribution of dust orbit eccentricity values (right). Created using minimum eccentricity $\epsilon_{\min} = 0.6$, and the ratio $a_{\text{moon}}/a_{\text{dust}} = 0.39$ for semimajor axes of dust and the moon. Angle α is measured clockwise from the apex direction, so that the values $-90° \leq (\alpha{+}180°) \leq 90°$ make up the leading side of the moon. The border between leading and trailing sides of the target moon is signified by the red dotted lines.

7, where the symmetric relation of the location of the two peaks compared to the apex direction is shown, as well as in the final contour plots that show a widely "spread out" maximum of dust flux on the trailing side of the moon (see figure 8).

The eccentricity of the example dust particle orbit presented in figure 6 is very high ($\epsilon = 0.8$), and the true anomaly at crossing locations is close to $f_1 \approx 90°$ and $f_2 \approx -90°$, where the radial velocity of dust is at its highest value ($\sin f = 1$ in equation 30). In the first crossing location ($f_1 > 0$, upper crossing point), the particle is approaching the moon from nearly jovian direction (from Jupiter), and in the second crossing location ($f_2 = -f_1$) the dust particle approaches the moon from nearly anti-jovian direction. The majority of the eccentricities of the simulated dust orbits are close to $\epsilon \approx 0.6$ value (see figure 7), and the impacts with the target moon should happen closer to the pericenter of the dust orbits (see also figure 4).

This means that some symmetric spreading or splitting of the flux maximum in two peaks is expected in the final contour plots, but the effect should not be drastic enough to cause the maximum flux to of dust to hit strictly from the jovian and anti-jovian directions.

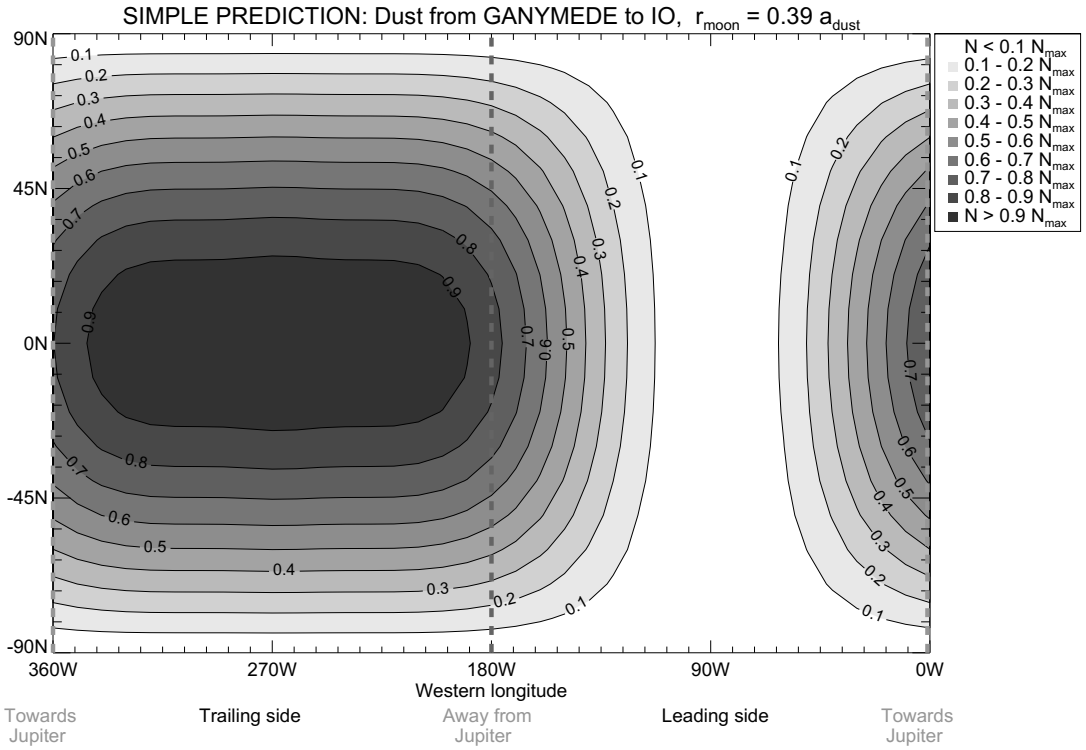

Figure 8: Contour plot showing the expected location of the leading-trailing anomalies on the surface of a target moon located interior to the Galilean dust ring. Created with the simple prediction model. The contour limits are presented as a relative fraction of the maximum flux value.

3.5.2 Target moon outside the dust ring

For a target moon located exterior to the dust source ($a_{\mathrm{moon}} > a_{\mathrm{dust}}$), the majority of the flux is expected on the leading side of the moon. In this situation, the dust grains cross the orbit of the target moon when they are close to the apocenter ($r_{\max}$, $f = 180°$) of their orbit (see figures 9 and 10), where their tangential velocity is lower than the local Kepler velocity (see figure 9). The same result is retrieved from equations (26-29):

$$v_{\mathrm{dust},\phi} < v_{\mathrm{Kepler}} \quad \text{when} \quad \cos f < 0. \tag{31}$$

Since the tangential velocity of dust is lower than the tangential velocity of the target moon, the particles impact the surface of the moon "from the front".

The total velocity of dust is low compared to the local Kepler velocity ($v_{\mathrm{Kepler}} >> v_{\mathrm{dust}}$) near the apocenter, so the radial velocity of dust $v_{\mathrm{dust},r}$ (see equation 30) is

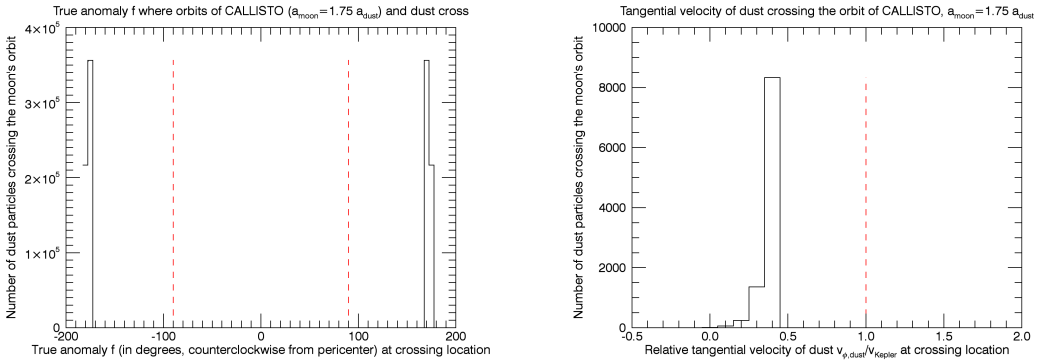

Figure 9: Histograms of the true anomaly f (left), and the relative tangential velocity of dust grains (right) at the crossing locations. The majority of dust particles originated from a dust ring interior to the orbit of the target moon cross the orbit of the moon near the apocenter ($f = 180°$) of their orbit, where their tangential velocity is lower than the local Kepler velocity ($v_{\phi,\mathrm{dust}}/v_{\mathrm{Kepler}} < 1$).

expected to be low compared to the relative tangential velocity of dust ($v_{\phi,\mathrm{dust}} - v_{\mathrm{Kepler}}$) as well. This means that the symmetric "splitting" of the dust flux peak in two should not be as significant as it was for a target moon located interior to the dust ring (see section 3.5.1), and the majority of the dust should be approaching the surface of the target moon from the apex direction.

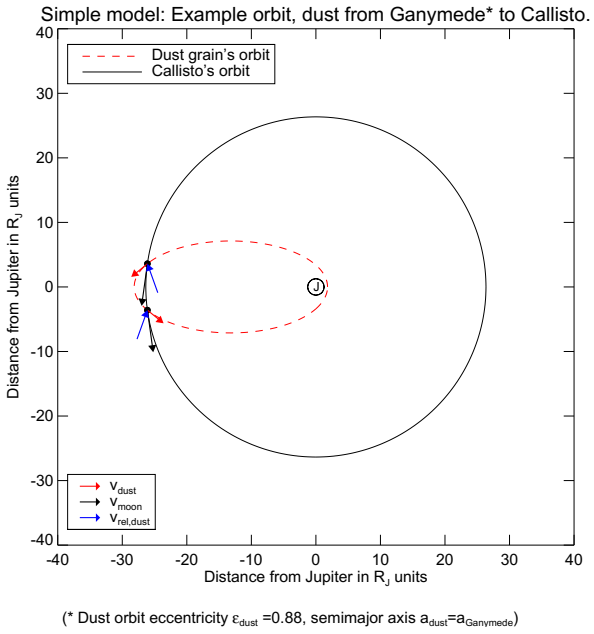

Figure 10: Example plot of the intersecting orbits of the moon Callisto, and a dust grain from Ganymede's distance.

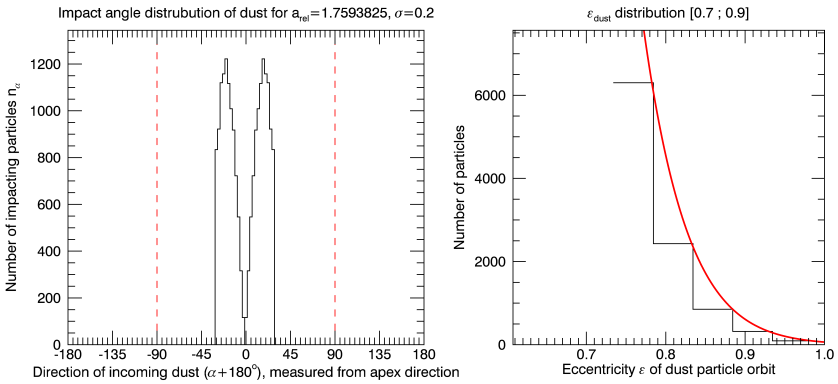

Figure 11: Distribution of impact angles for dust from Ganymede impacting the surface of Callisto (left), and the corresponding Rayleigh distribution of dust orbit eccentricity values (right). Created using minimum eccentricity $\epsilon_{\min} = 0.7$, and the ratio $a_{\text{moon}}/a_{\text{dust}} = 1.76$ for semimajor axes of dust and the moon. The angle α is measured clockwise from apex direction (direction of local Kepler velocity), so that the angles $-90° \leq (\alpha + 180°) \leq 90°$ make up the leading side of the moon. The border between leading and trailing sides of the target moon is signified by the red dotted lines.

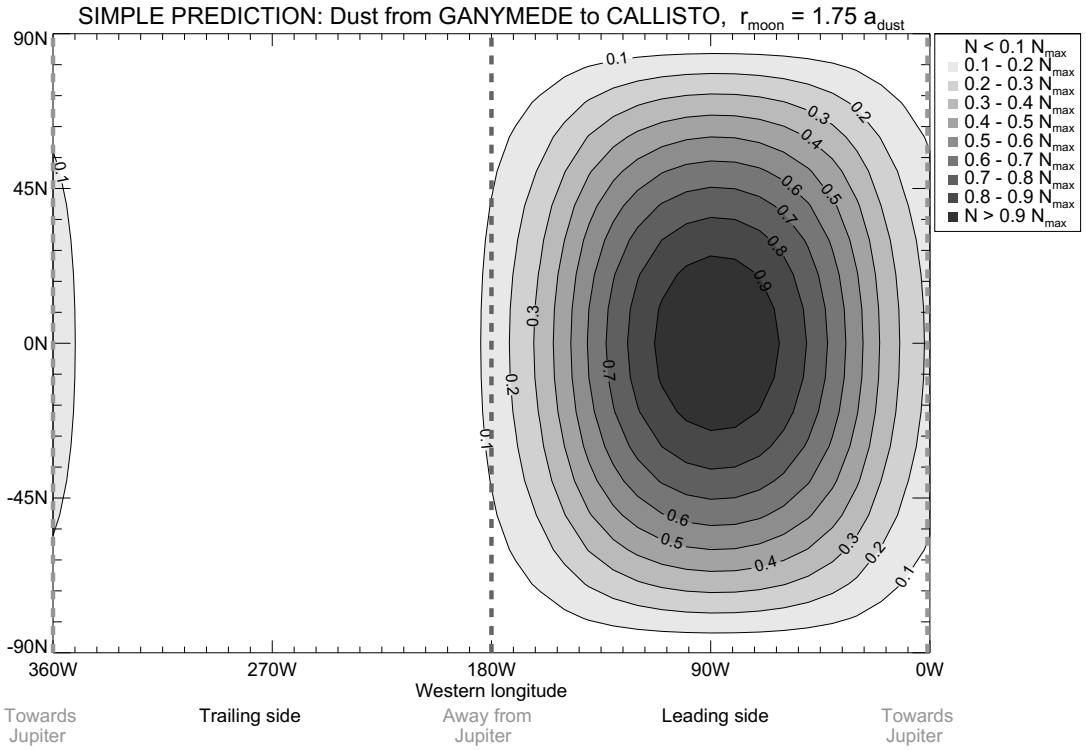

Figure 12: Contour plot showing the expected location of the leading-trailing anomalies on the surface of a target moon located exterior to the Galilean dust ring. Created with the simple prediction model. The contour limits are presented as a relative fraction of the maximum flux value.

3.5.3 Target moon at the distance of the dust ring

For a target moon located at the same distance from the planet as the dust source ($a_{\text{moon}} = a_{\text{dust}}$), a clear leading-trailing anomaly cannot be established. In this situation, the crossing locations are closer to $f_1 = 90°$ and $f_2 = -90°$ than to the pericenter or apocenter of the orbit. Near these values of f_1 and f_2, the tangential velocity of dust is close to the local Kepler velocity (see figure 13).

From the $v_{\text{dust},\phi}$ equation

$$v_{\text{dust},\phi} = v_{\text{Kepler}} \sqrt{1 + \epsilon \cos f}\,. \tag{32}$$

previously derived in section 3.5.1, we get that

$$v_{\text{dust},\phi} \approx v_{\text{Kepler}}\,, \quad \text{when} \quad \cos f \approx 0\,, \tag{33}$$

which is true for most simulated grains (see histogram of f values in crossing locations in figure 13).

Since the difference in the radial velocity of dust and the target moon is a more significant factor than the difference in tangential velocity, the peaks of incoming dust flux are expected in the jovian and anti-jovian directions on the surface of the moon.

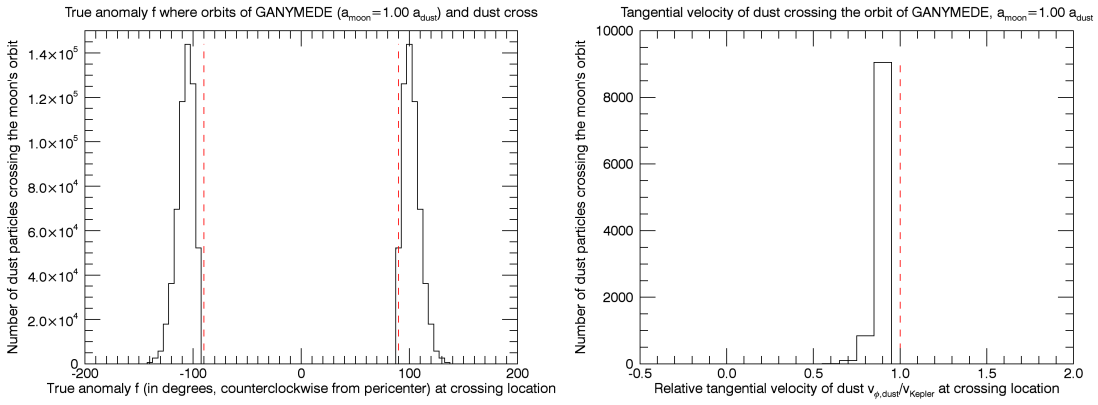

Figure 13: Histograms of the true anomaly f (left), and the relative tangential velocity of dust grains (right) at the crossing locations.

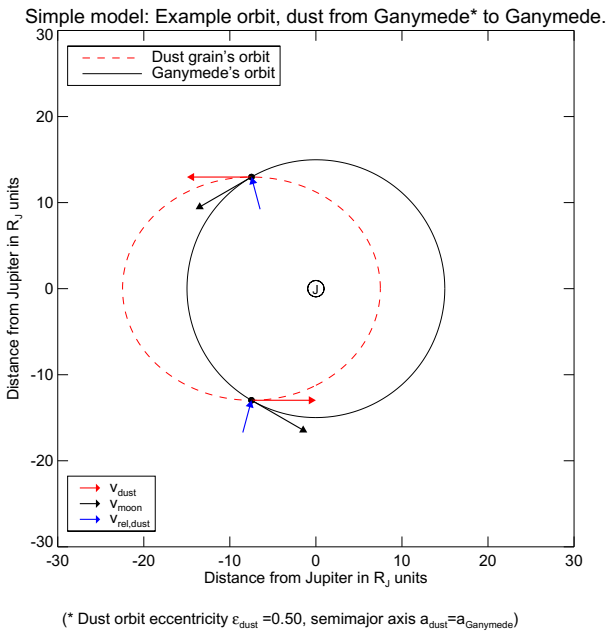

Figure 14: Example plot of the intersecting orbits of the moon Ganymede, and a dust grain from Ganymede's distance.

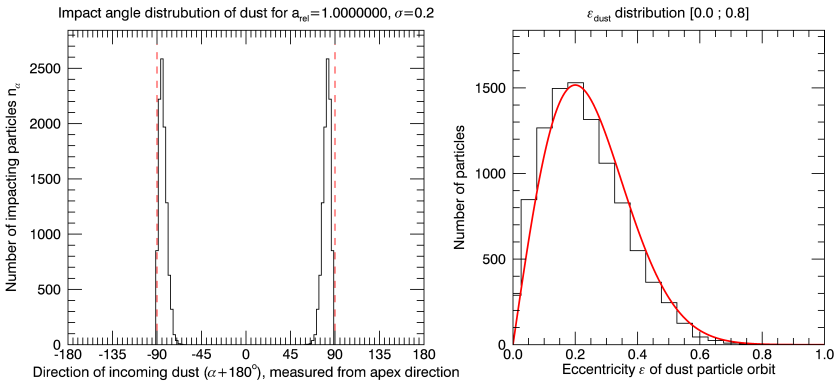

Figure 15: Distribution of impact angles for dust from Ganymede impacting the surface of Ganymede (left), and the corresponding Rayleigh distribution of dust orbit eccentricity values (right). Created using minimum eccentricity $\epsilon_{\min} = 0$, and the ratio $a_{\text{moon}}/a_{\text{dust}} = 1.0$ for semimajor axes of dust and the moon. The angle $(\alpha + 180°)$ is measured clockwise from apex direction (direction of local Kepler velocity), so that the angles $-90° \leq (\alpha + 180°) \leq 90°$ make up the leading side of the moon. The border between leading and trailing sides of the target moon is signified by the red dotted lines.

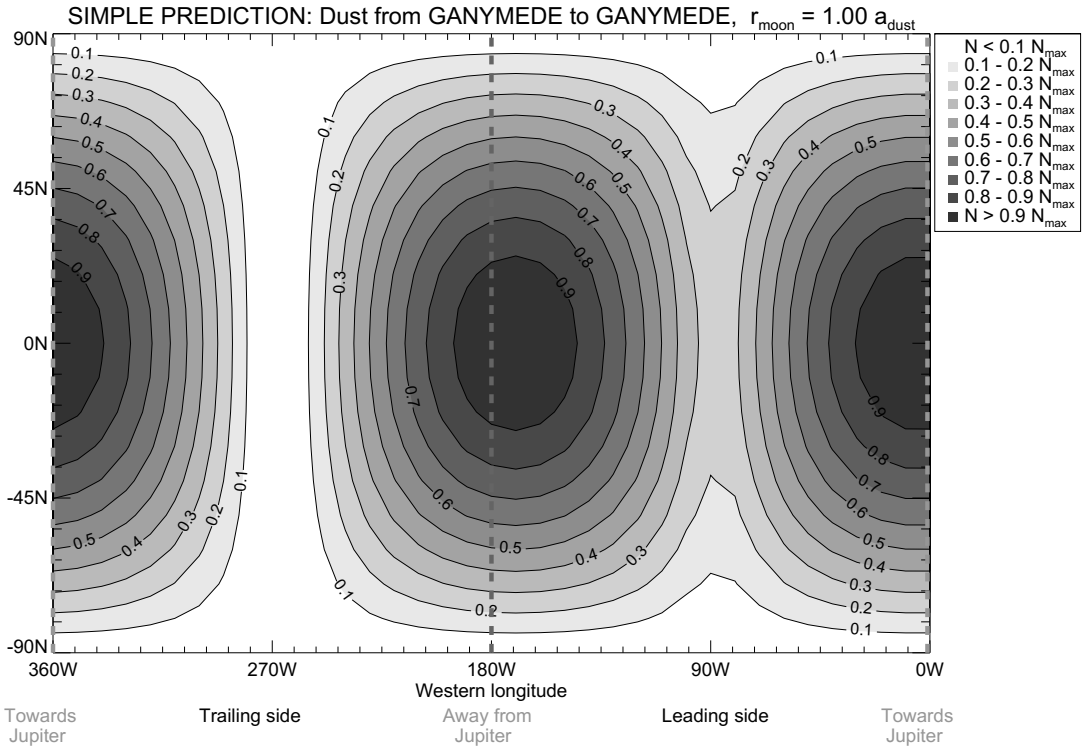

Figure 16: Contour plot showing the expected location of the leading-trailing anomalies on the surface of a target moon located inside the Galilean dust ring. Created with the simple prediction model. The contour limits are presented as a relative fraction of the maximum flux value.

4 Comparison to JMEM

4.1 Brief introduction to JMEM

The Jovian Meteoroid Environment Model (JMEM) was created at the Astronomy Research Unit of the University of Oulu for the European Space Agency between 2013 and 2016 by Xiaodong Liu and PI Jürgen Schmidt. The purpose of this model was to assess the dust hazard for spacecraft operating in the region of the Galilean moons [106].

JMEM uses a three-stage model for first describing the ejection of dust from the surface of the Galilean moons by high-velocity micrometeoroid impacts, then determining the escape locations and velocities of the dust grains from the Hill sphere of the moon, and lastly executing long-term integrations of the dust grain orbits under a variety of different forces acting on the grains in the Jupiter system

[8, 106].

As a result of these integrations, a jovicentric cylindrical dust density grid "dtab" was created. The cylinder grid is divided into $n_\phi = 40$ evenly distributed parts in the azimuthal direction, and to unevenly spaced grids in the radial and vertical directions. The radial grid is divided into $n_R = 73$ parts between [$1R_J$, $120R_J$] distance from Jupiter. The radial grid is most resolved in the vicinity of the Galilean moons. Most of the radial grid lines (68 out of 73) lie between $[2R_J, 33R_J]$ distance from Jupiter, where the grid is defined in a logarithmic manner. The Z-grid covers vertical distances between $[-50R_J, +50R_J]$ measured from the equatorial plane of Jupiter, consisting of $n_Z = 29$ parts. The vertical grid is better resolved near the equatorial plane of Jupiter, where the dust density and its gradients generally are the greatest.

Each of these cylinder grid cells contains information about the local number density of the dust particles orbiting Jupiter, and the first three moments of the velocity components in three dimensions. JMEM reconstructs a 3-dimensional approximation to velocity distribution in each grid cell from the stored density and the velocity moments. The velocity distribution is used to determine dust fluxes on a given surface in the system (equation 35). The data in the dtab files comes from long-term numerical integrations of a large number of trajectories of dust particles launched from each moon (see Liu et al [2] for details). Integrations use large number of gravitational and non-gravitational perturbation forces acting on dust particles. Calibration of the model is done using *in situ* measurements from the Galileo DDS [28].

Main parameters in the JMEM model are the slope q of ejecta size distribution $f(r_{\mathrm{g,min}})$, two models for the ejecta size distribution (either a single value of q or a broken power law with q_1 and q_2 parts), two modes of possible DDS calibration s_{calib}, and the lower cut-off radius s_0 chosen to evaluate the cumulative number density $N(> s_0)$.

We use here an ejecta size distribution in form of a power law normalized in the size range $[r_{\mathrm{g,min}}, \infty]$, presented in its differential form as

$$f(r_g) = c r_g^{-q}\,, \tag{34}$$

where c is a constant depending on the normalization.

For the majority of contour plots generated in section 4.3, the value $q = 3.7$ is chosen for the slope of ejecta size distribution, based on the Lunar Dust Experiment (LDEX) measurements of a dust cloud around Luna [107]. In the JMEM model itself, a more conservative estimate of $q = 3.4$, supported by Galileo DDS measurements near the Galilean moons [47], is favored to avoid underestimating the flux of larger particles in the Jupiter system. For the purpose of assessing dust hazard for spacecraft operating in the region of the Galilean moons, erring on

the side of caution is critically important. For estimating the dust fluxes on the surface of the Galilean moons, using the more recent estimate by LDEX instead is (arguably) a reasonable choice.

The effect of a broken power law for the ejecta size distribution, introduced in the JMEM model [8, 108], is briefly shown in section 4.3.5. In both the meteoroid engineering model (MEM) by NASA [109] and the interplanetary meteoroid environment (IMEM) model by ESA [110], there is a knee in the size distribution of interplanetary meteoroids around 100μm, so that the slope of the size distribution of meteoroids is steeper for larger particle sizes. These models are more constrained with data from the inner solar system, but if this knee in the impactor population is present at Jupiter distance as well, it should be inherited by the ejecta size distribution, so that there is a reduction in the amount of ejected larger dust grains. The majority of the ejected dust should consist of moderate grain sizes around 1μm in radius, so the effect of the broken power law should not be a major factor in the number fluxes of dust on the Galilean moons, and in this thesis we mostly use a single, continuous power law for the size distribution.

The s_{calib} parameter, the minimum detected particle size of DDS, is used in calibrating the JMEM results to the *in situ* measurements of the Galileo dust detector. The value of this parameter could be estimated as either $s_{\text{calib}} = 0.3\mu$m [52] or $s_{\text{calib}} = 0.6\mu$m [28]. In the majority of the contour plots in 4.3, the more sensitive threshold of $s_{\text{calib}} = 0.3\mu$m is assumed.

For the minimum cut-off size s_0 for displaying the cumulative number density of dust $N(> s_0)$, there exists 13 available options between $0.05\mu\text{m} - 1\text{cm}$ in the JMEM model. A subarray of these sizes is chosen for the final plots presented in section 4.3.3.

4.2 Application of JMEM to evaluate maps of dust fluxes hitting the surfaces of the Galilean moons

JMEM can evaluate the cumulative flux (number of particles larger than a given size per second and per square meter) using the following kinetic integral:

$$J(\bar{k}, \bar{x}, \bar{v}_{sc}, > s) = \int d^3v f_{\bar{x}}(\bar{v}, > s)(\bar{v}_{sc} - \bar{v}) \cdot \bar{k}\, \Theta_H((\bar{v}_{sc} - \bar{v}) \cdot \bar{k})\,, \qquad (35)$$

where $f_{\bar{x}}$ describes the dust velocity distribution function at location $\bar{x}$ for particles of radius larger than s. This function is normalized to the particle number density at $\bar{x}$, so that its dimension is $\frac{1}{\text{m}^3\left(\frac{\text{m}}{\text{s}}\right)^3}$. The lower size limit s of dust particles can be chosen from the 13 possible values included in the model: 0.05μm, 0.1μm, 0.3μm, 0.6μm, 1μm, 2μm, 5μm, 10μm, 30μm, 100μm, 300μm, 1000μm, 1cm. $\bar{v}_{\text{sc}}$ is the velocity vector of the test surface (or the velocity of the spacecraft moving relative

to the dust), and the vector $\bar{k}$ denotes the surface normal of the test surface. Taking a dot product with the $\bar{k}$-vector takes into account the orientation of the surface element (the effect of reduced crosscut area for a dust stream approaching a tilted surface, non-perpendicular to the direction of relative velocity). The symbol Θ_H denotes the Heaviside step function, which ensures that only particles approaching the surface from the front are counted.

The contour plots are created by dividing the surface of the moons to longitude-latitude (ϕ, θ) grids (identical to the surface grid used in the model described in section 3.3, see figure 3) and evaluating the flux integral (35) for each of the surface elements of orientation $\bar{k}(\phi, \theta)$, moving through a dust distribution $f_{\bar{x}}(\bar{v})$ with velocity $\bar{v}_{sc} = \bar{v}_{Kepler}$ relative to the inertial Jupiter centered frame (the low additional velocity of the element due to rotation of the moons is neglected). Using a fixed longitude-latitude coordinate system for the surface elements, relative to the Jupiter direction, is possible since (as described in section 3.4) the Galilean moons are in a state of bound rotation.

The value of the dust velocity distribution function $f_{\bar{x}}$ at the desired location is retrieved from the cylindrical dtab grid in JMEM by trilinearly interpolating the stored values of the velocity distribution and number density at the center of the dtab grid cell the moon is located at, and the values of the six neighbouring cells, according to the relative position of the moon inside the cell. The velocity distribution function is then numerically integrated over the relative velocity of dust in three dimensions.

For simplicity, all the surface elements of the moon are placed at the center of mass of the moon, and only their orientation is varied according to the position on a sphere for their latitude and longitude. This means, that we neglect the effect of the moon's finite size on the evaluation of the flux. This is a good approximation, because the typical distances over which the dust number density changes in the system is much larger than the moon diameter.

4.3 Results: Longitude-latitude maps of impact-generated dust fluxes on the Galilean moons

The results from JMEM are presented as contour plots similar to those generated in the simple model in section 3.5. In these plots, x-axis is the Western Longitude WL on the surface of the moon, measured clockwise from the Jupiter direction WL = 0, so that the values $0° < \mathrm{WL} < 180°$ make up the leading side of the moon, and the values between $180° < \mathrm{WL} < 360°$ make up its trailing side. The y-axis of these plots is the Northern Latitude NL, measured from the equator of the target moon NL = 0° so that the value NL = +90° represents the "north pole" of the moon, and NL = −90° is its "south pole" (see coordinate system described

in section 3.4, and figure 3).

The fluxes on the surface of the moons in the contour plots of sections 4.3.1-4.3.5 are presented in SI units as the number of impacting particles per square meter and per second. In section 4.3.6 the total fluxes on the surface of the moons are estimated as the number of impacting particles per second.

4.3.1 Effect of azimuthal position of the moon in the Jupiter system

Mapping the dust fluxes on individual points in a moon's orbit revealed relatively strong azimuthal variations in the dust density and velocity distribution in the cylindrical dtab grid of JMEM. For each of the four moons the JMEM model exhibits individual points in their orbit, corresponding to specific grid cells in JMEM, where the locations of minimum and maximum fluxes even would abruptly be "reversed" compared to neighbouring points on the orbit. Instead of consistently getting most of the particle flux on the leading or trailing side of the moon, there would suddenly be a strong flux on the north or south pole of the moon, or in the jovian or antijovian direction. This feature is especially pronounced for the smaller particle sizes in the model.

In figure 17 an example section of one such orbit with sudden azimuthal variations is presented for the moon Europa. The instantaneous location and velocity of the moon is retrieved from the NAIF SPICE toolkit for IDL (provided by NASA's Jet Propulsion Laboratory (JPL)) for 40 individual points in orbit, using a constant time step $dt = P_{\mathrm{orb}}/40$ and starting (arbitrarily) from the J2000 epoch.

The azimuthal variations seen in the plots created for individual points in orbit are not actually expected in the Jupiter system, and are a result of spurious variations in the JMEM model instead. There is indeed an azimuthal aymmetry of dust in the region of Galilean moons predicted in the model [2], but that asymmetry becomes apparent only when the dust configuration is evaluated in a Jovicentric frame that keeps a fixed orientation with respect to the Sun. For the purpose of this thesis, the fluxes have not been evaluated from such dtab files that keep a fixed orientation with respect to the Sun. The creation of these dtab files is currently in progress (by Liu, see [2] for initial details), and they can be utilized at a later step. For the time being, it is sufficient to concentrate on the azimuthally averaged plots, which have the added benefit of being directly comparable to the model presented in chapter 3.

The orbit-averaged plots, created by averaging the results for 40 individual points in orbit (see figure 18 for an example of such plot generated from single-point results) are significantly smoother and more meaningful than the azimuthally resolved plots, so for the rest of the results (sections 4.3.2-4.3.5), only the orbit-averaged plots are used.

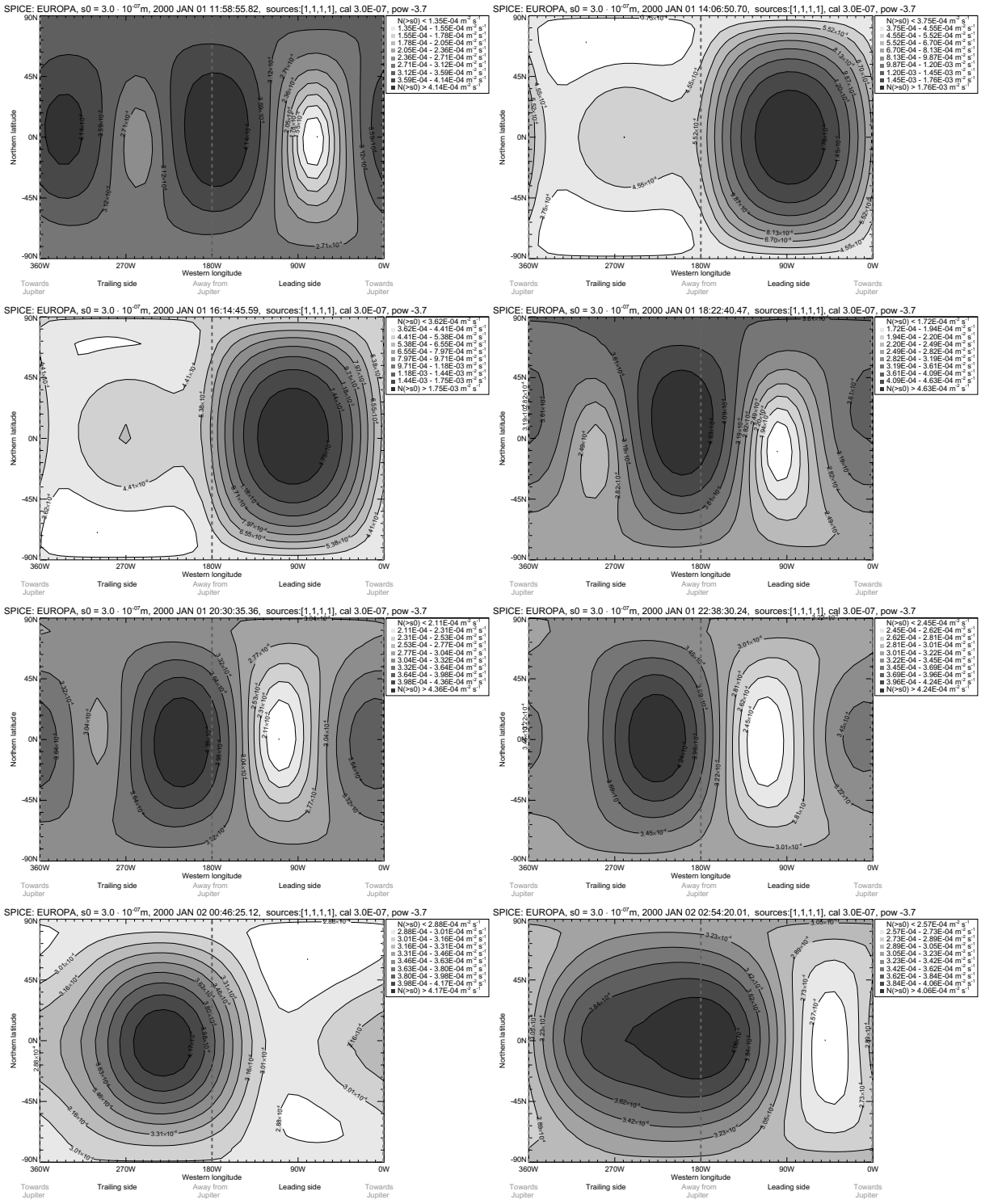

Figure 17: Dust fluxes at individual points in the orbit of the moon Europa. Locations and velocities retrieved from SPICE, starting from the J2000 epoch, and using a constant time step of $P_{orbit}/40$ (points 1-8 out of 40 are shown).

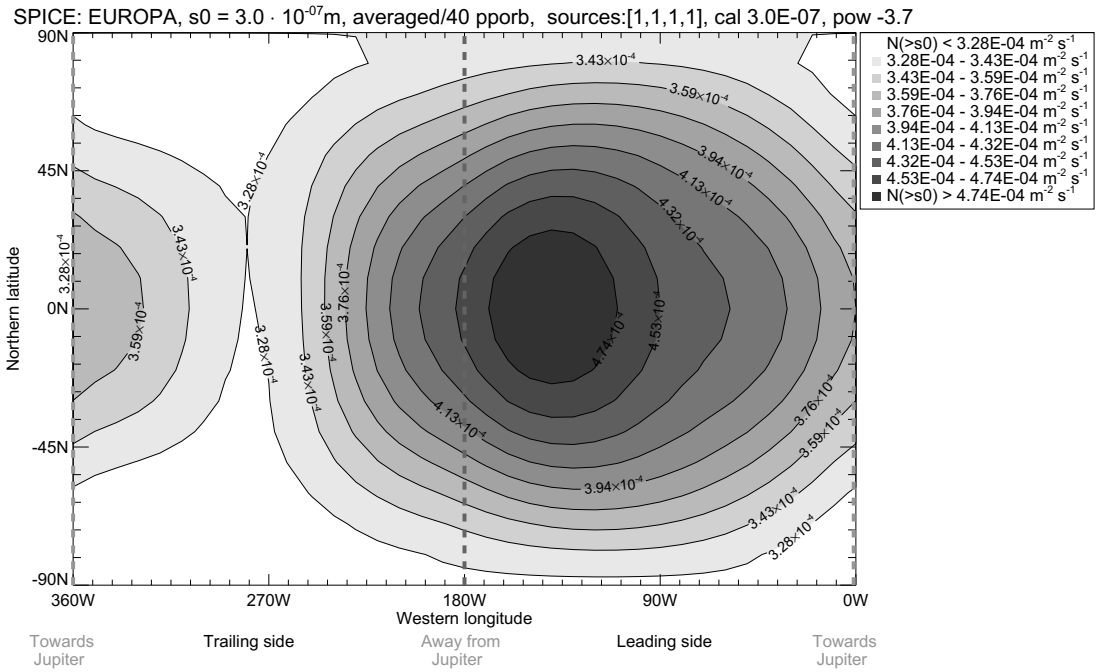

Figure 18: Orbit-averaged plot for number flux of dust particles on the surface of Europa. Created by averaging over 40 locations on the moon orbit.

4.3.2 Comparison of fluxes on the surface of different moons

In figure 19, the cumulative number flux $N(> s_0)$ of dust particles larger than $s_0 = 0.3\mu$m, ejected from all four Galilean moons, is presented for each target moon. The default values of DDS calibration $s_{\text{calib}} = 0.3\mu$m, and an ejecta size distribution with a single value of the exponent $q = 3.7$ are used for all plots in this subsection. The largest ($N_{\max}$) and smallest ($N_{\min}$) flux values on the surface of the moons in these contour plots are given in table 1.

Target:	Io	Europa	Ganymede	Callisto
$N_{\min}$	$7.62 \cdot 10^{-5} \frac{1}{\text{m}^2\text{s}}$	$3.13 \cdot 10^{-4} \frac{1}{\text{m}^2\text{s}}$	$6.15 \cdot 10^{-5} \frac{1}{\text{m}^2\text{s}}$	$1.43 \cdot 10^{-5} \frac{1}{\text{m}^2\text{s}}$
$N_{\max}$	$3.75 \cdot 10^{-4} \frac{1}{\text{m}^2\text{s}}$	$4.96 \cdot 10^{-4} \frac{1}{\text{m}^2\text{s}}$	$2.49 \cdot 10^{-4} \frac{1}{\text{m}^2\text{s}}$	$7.91 \cdot 10^{-5} \frac{1}{\text{m}^2\text{s}}$

Table 1: Minimum and maximum values of cumulative dust number flux $N(> 0.3\mu\text{m})$ on the surface of the Galilean moons in the contour plots of figure 19.

From figure 19 and table 1 it is seen, that the flux of particles larger than 0.3μm, detached from the surface all four source moons, is at its largest value on the surface of Europa, where the majority of the flux impacts on the leading

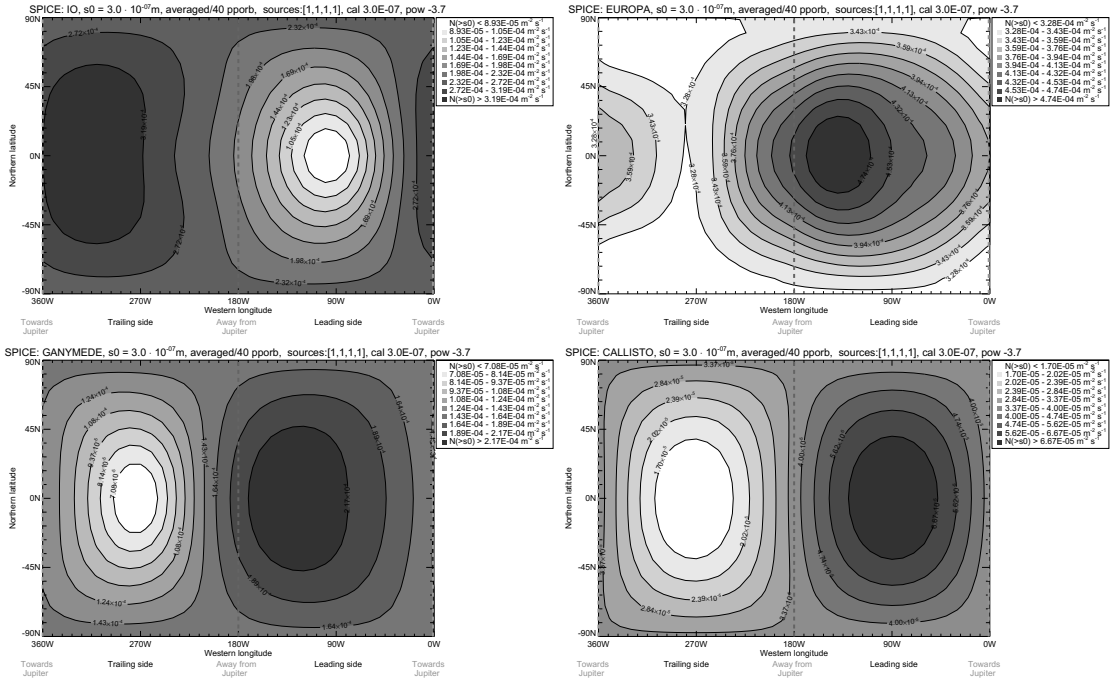

Figure 19: The number flux ($\frac{1}{\mathrm{m^2 s}}$) of particles larger than $s_0 = 0.3\mu$m, ejected from all four Galilean moons, impacting on the surface of Io (top left), Europa (top right), Ganymede (bottom left) and Callisto (bottom right).

side of the target moon. The minimum N_{min} and maximum N_{max} values of the cumulative dust flux on the surface of the moon are very close to each other ($N_{\mathrm{min,Europa}} \approx 0.63 N_{\mathrm{max,Europa}}$).

The maximum value of flux on Io is roughly of the same order of magnitude as the maximum value of flux on Europa ($N_{\mathrm{max,Io}} \approx 0.75 N_{\mathrm{max,Europa}}$). The majority of the flux hits Io on its trailing side. On Ganymede the maximum value of flux is about half of that on Europa ($N_{\mathrm{max,Ganymede}} \approx 0.50 N_{\mathrm{max,Europa}}$). The overall weakest flux is seen on the surface of Callisto, where the highest flux value is less than 1/6 of the N_{max} on Europa ($N_{\mathrm{max,Callisto}} \approx 0.16 N_{\mathrm{max,Europa}}$). On both Ganymede and Callisto, the majority of the flux hits the moons on their leading side.

In general, the difference between the minimum and maximum value of the flux on all of the moons is surprisingly small, the maximum value being at most a factor of 5 larger ($N_{\mathrm{max,Callisto}} \approx 5.5 N_{\mathrm{min,Callisto}}$) than the corresponding minimum value on the surface of the target moon in question.

To compare these results with the predictions made with the simple model, some knowledge about the radial density profile of the Galilean ring, and the relative locations of the moons in regards to the dust ring, is needed. In figure

20, a mid-cut density plot of the ring plane, taken from the JMEM graphical user interface, is presented.

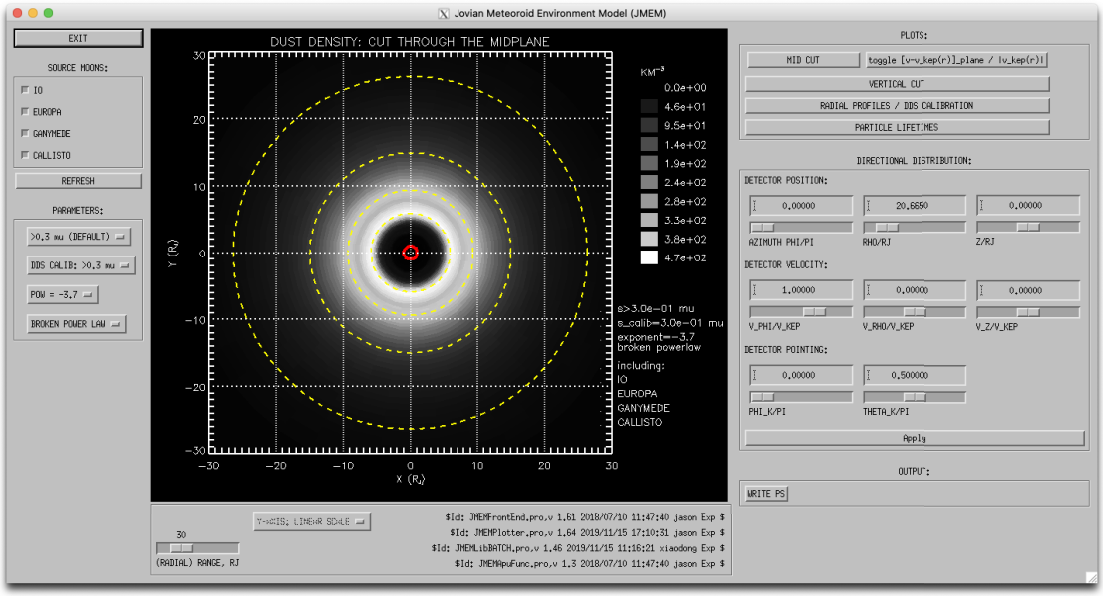

Figure 20: Midplane dust density plot from JMEM, showing the orbits of the four Galilean moons (yellow dashed lines), and the dust density at different radial distances from Jupiter. The peak value of the density of the Galilean ring is located slightly inside the orbit of Europa.

The majority of the dust material in the Galilean ring is concentrated between the innermost Galilean moons Io and Europa. The peak of the dust density is located slightly inside the orbit of Europa, so it can be stated that Io is located "interior to the dust ring", Europa is located "at the distance of the dust ring", and Ganymede and Callisto are "exterior to the dust ring".

Based on predictions from the model in section 3, this would mean that the moon Io should have a maximum on its trailing side, Europa should have a strong flux at its jovian and anti-jovian directions, and Ganymede and Callisto should receive the majority of their flux on their leading side. For the most part, the contour plots generated in figure 19 follow this logic. However, the "spreading" or "splitting" of the peaks on the leading and trailing sides of the moons, predicted in section 3.5, is not noticeable here. Additionally, for Europa, the majority of the flux is seen on its leading side instead of the expected strong anomalies in the jovian and anti-jovian directions.

From these slight differences we see that the behaviour of the smallest, sub-micron particle sizes in JMEM does not strictly compare to the basic Keplerian

principle behind leading-trailing anomalies on the surface of the moons presented in section 3.5. To achieve a more meaningful comparison between the two models, an additional set of contour plots for cumulative dust flux of $> 1\mu$m grain sizes is created in figure 21.

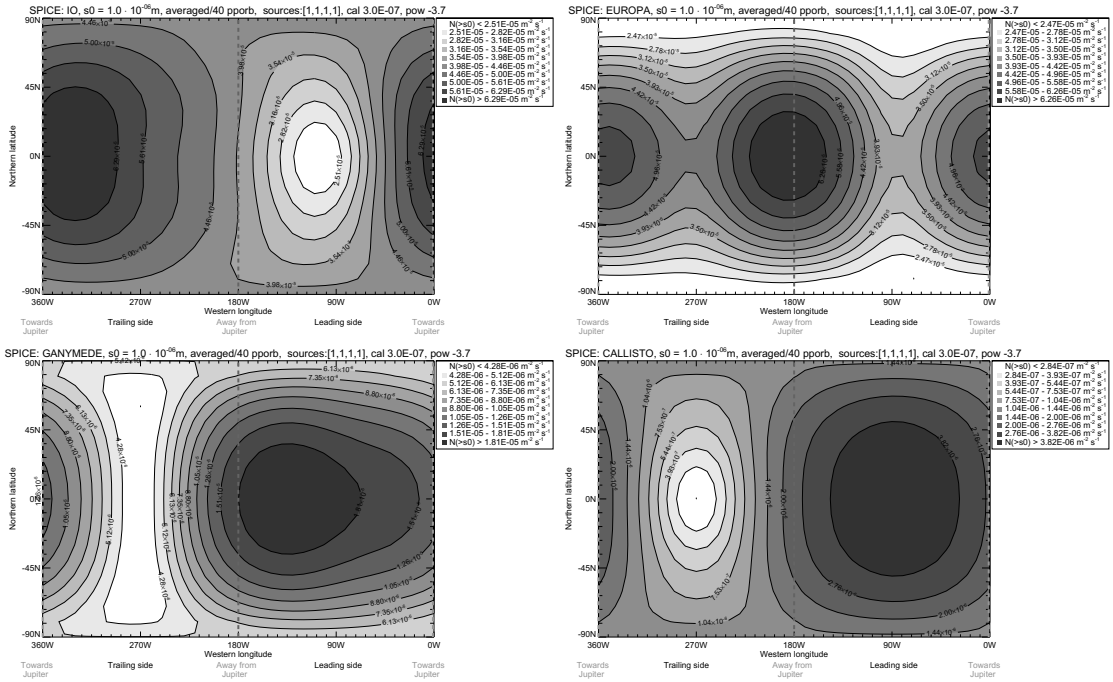

Figure 21: The number flux of particles larger than $s_0 = 1\mu$m, ejected from all four Galilean moons, impacting on the surface of Io (top left), Europa (top right), Ganymede (bottom left) and Callisto (bottom right).

Target:	Io	Europa	Ganymede	Callisto
$N_{\min}$	$2.24 \cdot 10^{-5} \frac{1}{\mathrm{m^2 s}}$	$2.20 \cdot 10^{-5} \frac{1}{\mathrm{m^2 s}}$	$3.57 \cdot 10^{-6} \frac{1}{\mathrm{m^2 s}}$	$2.05 \cdot 10^{-7} \frac{1}{\mathrm{m^2 s}}$
$N_{\max}$	$7.06 \cdot 10^{-5} \frac{1}{\mathrm{m^2 s}}$	$7.03 \cdot 10^{-5} \frac{1}{\mathrm{m^2 s}}$	$2.17 \cdot 10^{-5} \frac{1}{\mathrm{m^2 s}}$	$5.29 \cdot 10^{-6} \frac{1}{\mathrm{m^2 s}}$

Table 2: Minimum and maximum values of cumulative dust number flux $N(> 1\mu$m) on the surface of the Galilean moons in the contour plots of figure 21.

For grain sizes larger than 1 micron, the basic principle, suggested by the model, behind the leading-trailing anomalies on the surface of the moons is better reflected. For Europa, which is located roughly where the density of the Galilean ring is the highest, a clear maximum of the flux coming from the jovian and anti-jovian directions on the surface of the moon is now shown. On the leading side of

Ganymede, some "spreading" of the peak of maximum flux (described in section 3.5) is also noticeable.

4.3.3 Effect of minimum dust particle size

In figure 22, maps of the cumulative number flux $N(> s_0)$ of dust particles impacting on the surface of Ganymede is shown for a chosen array of minimum sizes $s_0 = 0.3\mu$m, $s_0 = 0.6\mu$m, $s_0 = 1\mu$m, and $s_0 = 5\mu$m. The smallest available particle sizes available in the model (between 0.05μm-0.3μm) are ignored, as the JMEM model is not equipped to portray their behaviour particularly well. Similarly, the largest options for minimum size (from $> 10\mu$m to $>$ 1cm grains) are not used, as the production rate of these larger grains is very sporadic and uncertain, and the flux rate of these particles might not be very accurate in the model.

Table 3 shows the minimum and maximum values of flux on the surface of Ganymede, corresponding to contours of figure 22. The default values of DDS calibration $s_{\mathrm{calib}} = 0.3\mu$m, and an ejecta size distribution with a single value of the power law exponent $q = 3.7$ are used for all plots throughout this subsection.

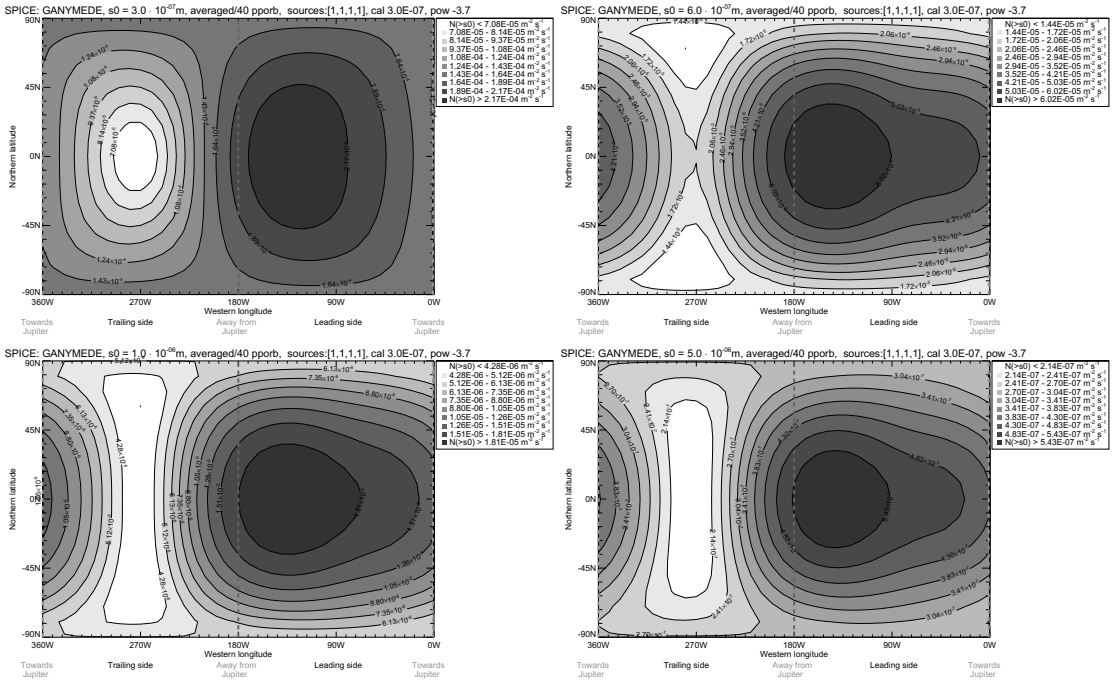

Figure 22: Cumulative dust flux $N(> s_0)$ of particles larger than $s_0 = 0.3\mu$m (top left), $s_0 = 0.6\mu$m (top right), $s_0 = 1\mu$m (bottom left), and $s_0 = 5\mu$m (bottom right) on the surface of Ganymede.

Min. size	$s_0 = 0.3\mu$m	$s_0 = 0.6\mu$m	$s_0 = 1\mu$m	$s_0 = 5\mu$m
$N_{\min}$	$6.15 \cdot 10^{-5} \frac{1}{\mathrm{m^2 s}}$	$1.20 \cdot 10^{-5} \frac{1}{\mathrm{m^2 s}}$	$3.57 \cdot 10^{-6} \frac{1}{\mathrm{m^2 s}}$	$1.91 \cdot 10^{-7} \frac{1}{\mathrm{m^2 s}}$
$N_{\max}$	$2.49 \cdot 10^{-4} \frac{1}{\mathrm{m^2 s}}$	$7.20 \cdot 10^{-5} \frac{1}{\mathrm{m^2 s}}$	$2.17 \cdot 10^{-5} \frac{1}{\mathrm{m^2 s}}$	$6.10 \cdot 10^{-7} \frac{1}{\mathrm{m^2 s}}$

Table 3: Minimum and maximum values of cumulative dust number flux $N(> s_0)$ on the surface of Ganymede, for an array of different minimum sizes s_0 used in contour plots of figure 22.

From table 3 we see that the cumulative flux drastically decreases as the minimum size of dust is increased. This is not surprising, as the size distribution of dust impacting on the surface of the moons follows from the power law of the size distribution of ejected dust material in first place, modified by the orbital dynamics and lifetimes of the grains. The most significant drop in the cumulative number flux is seen here for particles larger than 1 micron in radius.

The minimum grain size s_0 does not seem to have much of an effect on the location of minimum and maximum fluxes on the target moon. The only noticeable difference in the shape of the contours is, that for grain sizes larger than 0.6μm, the peak on the leading side of Ganymede is somewhat more spread out towards the Jupiter direction as well, compared to the peak of cumulative flux for $> 0.3\mu$m particles located between the anti-jovian and apex directions.

4.3.4 Dust from individual source moons

In figure 23, the individual contributions of the four Galilean moons to the cumulative number flux $N(> s_0)$ of dust particles larger than $s_0 = 0.3\mu$m impacting on the surface of Ganymede are shown. The default values of DDS calibration $s_{\mathrm{calib}} = 0.3\mu$m, and an ejecta size distribution with a single value of the power law exponent $q = 3.7$ are used for all plots in this subsection. The minimum and maximum values of flux on the surface of Ganymede are shown in table 4.

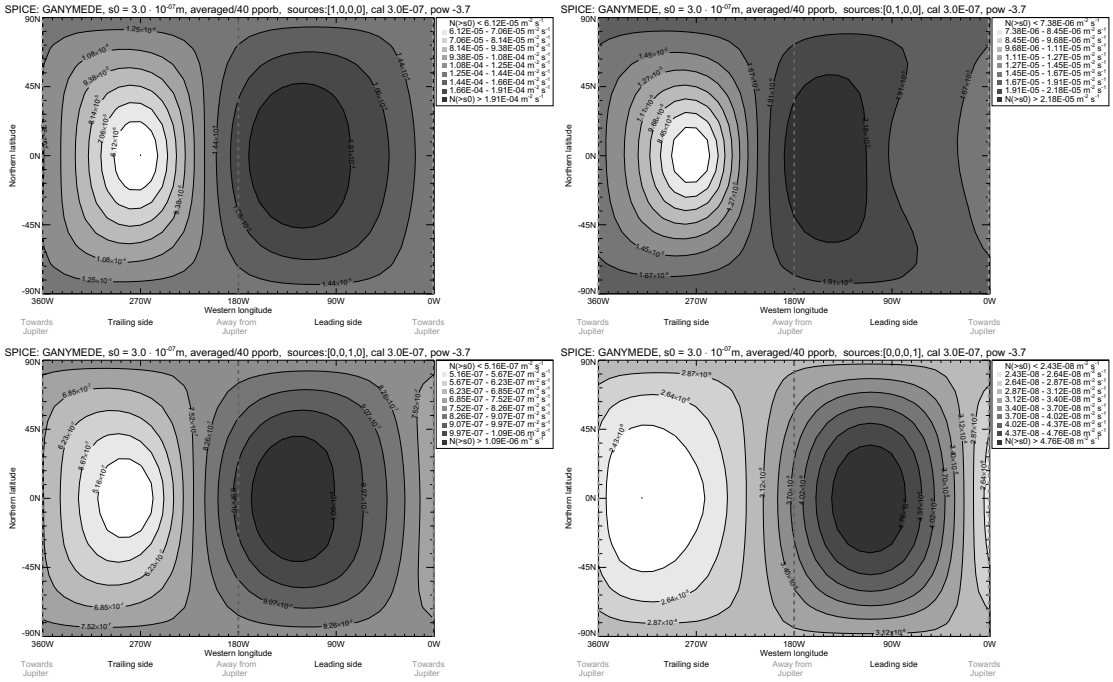

Figure 23: Cumulative dust flux $N(> 0.3\mu\text{m})$ from individual source moons Io (top left), Europa (top right), Ganymede (bottom left) and Callisto (bottom right), impacting on the surface of Ganymede.

Source:	Io	Europa	Ganymede	Callisto
$N_{\min}$	$5.31 \cdot 10^{-5} \frac{1}{\text{m}^2\text{s}}$	$6.44 \cdot 10^{-6} \frac{1}{\text{m}^2\text{s}}$	$4.70 \cdot 10^{-7} \frac{1}{\text{m}^2\text{s}}$	$2.23 \cdot 10^{-8} \frac{1}{\text{m}^2\text{s}}$
$N_{\max}$	$2.20 \cdot 10^{-4} \frac{1}{\text{m}^2\text{s}}$	$2.50 \cdot 10^{-5} \frac{1}{\text{m}^2\text{s}}$	$1.20 \cdot 10^{-6} \frac{1}{\text{m}^2\text{s}}$	$5.17 \cdot 10^{-8} \frac{1}{\text{m}^2\text{s}}$

Table 4: Minimum and maximum values of cumulative dust number flux $N(> s_0)$ on the surface of Ganymede, from individual source moons (see figure 23).

The vast majority of the dust flux impacting on the surface of Ganymede is originated from Io (see figure 23 and table 4). Flux from Europa is an order of magnitude lower compared to Io as a dust source, but still significant compared to the dust originated from the outer Galilean moons Ganymede and Callisto. The grains from Ganymede re-impacting on the surface, and dust from Callisto form a nearly insignificant minority of the dust impacting on Ganymede.

A slightly odd or unexpected result is seen on the bottom right contour plot of figure 23. In the model of section 3.5, it was predicted that dust grains from outside the target moon's distance $a_{\text{moon}} < a_{\text{dust}}$ should impact the moon on its trailing side. Here a clear maximum on the leading side of the moon is shown instead. However, changing the minimum grain size to a higher value of $s_0 = 5\mu\text{m}$

produces results that are a bit more in line with the Keplerian model (see figure 24).

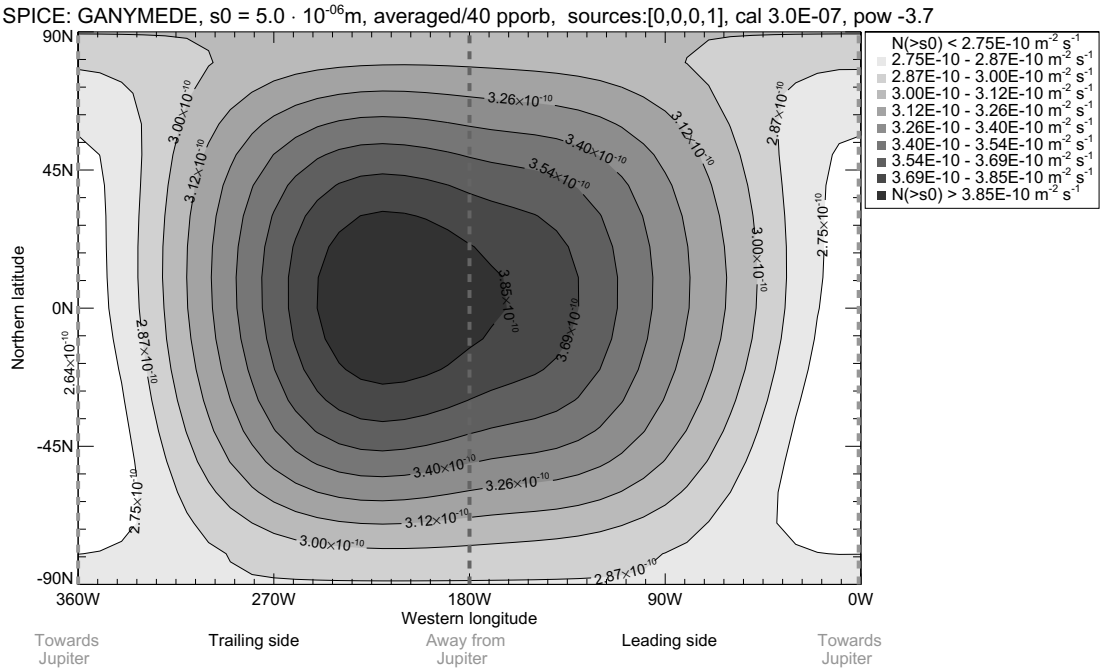

Figure 24: Cumulative dust flux from Callisto, impacting on the surface of Ganymede, using minimum grain size of $s_0 = 5\mu$m.

In figure 25, a similar sequence of plots is created for the moon Europa. Table 5 shows the corresponding minimum and maximum values of flux on the surface of the moon.

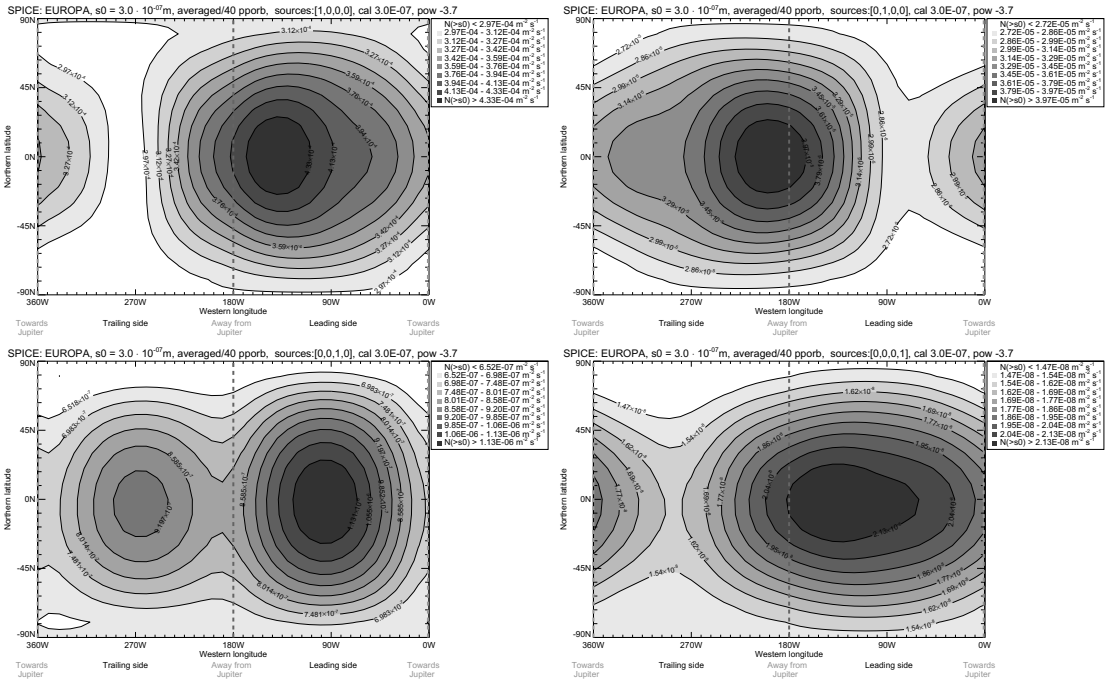

Figure 25: Cumulative dust flux $N(> 0.3\mu\text{m})$ from individual source moons Io (top left), Europa (top right), Ganymede (bottom left) and Callisto (bottom right), impacting on the surface of Europa.

Source:	Io	Europa	Ganymede	Callisto
$N_{\min}$	$2.84 \cdot 10^{-4} \frac{1}{\text{m}^2\text{s}}$	$2.60 \cdot 10^{-5} \frac{1}{\text{m}^2\text{s}}$	$6.08 \cdot 10^{-7} \frac{1}{\text{m}^2\text{s}}$	$1.41 \cdot 10^{-8} \frac{1}{\text{m}^2\text{s}}$
$N_{\max}$	$4.54 \cdot 10^{-4} \frac{1}{\text{m}^2\text{s}}$	$4.16 \cdot 10^{-5} \frac{1}{\text{m}^2\text{s}}$	$1.21 \cdot 10^{-6} \frac{1}{\text{m}^2\text{s}}$	$2.24 \cdot 10^{-8} \frac{1}{\text{m}^2\text{s}}$

Table 5: Minimum and maximum values of cumulative dust number flux $N(> s_0)$ from individual source moons, impacting on the surface of Europa (see figure 25).

Similar to the situation for Ganymede, flux from Io is the most significant source of dust impacting on the surface of Europa as well. The overall flux on Europa is larger than on Ganymede, which is understandable, since Europa is located inside the densest part of the Galilean ring. Again, the flux of dust from the source moons located outside the orbit of Europa does not seem to follow the predicted placements of minimum and maximum fluxes of dust. Limiting the cumulative flux to particles larger than 5μm flips the location of maxima around for particles coming from Ganymede, but does not seem to have much of an effect on the particles originated from Callisto (see figure 26). Perhaps the flux of dust from Callisto is overall so low (generally around two orders of magnitude lower than the flux from other Galilean moons, see tables 4-5), that the effect of individual

dust grains is more significant, stochastic variation is fairly large, and the flux is less smoothly distributed.

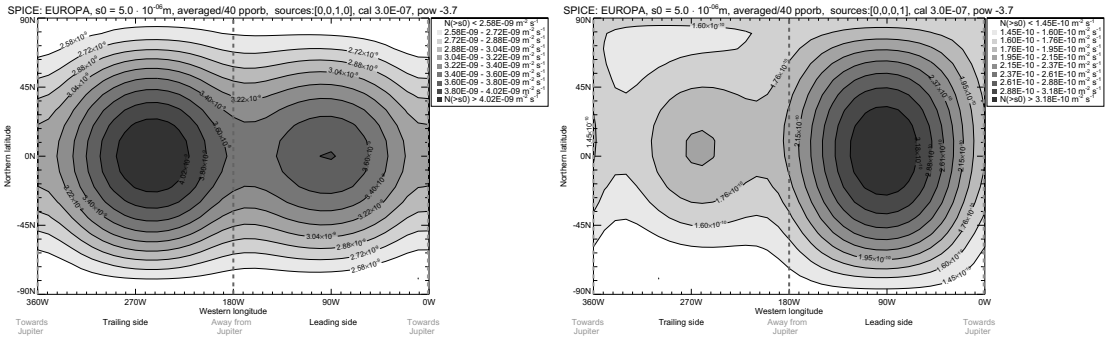

Figure 26: Cumulative dust flux from Ganymede (left) and Callisto (right), impacting on the surface of Europa, using minimum grain size of $s_0 = 5\mu$m.

4.3.5 Effect of DDS calibration, ejecta distribution exponent, and broken power law

In figure 27, the cumulative number flux $N(> s_0)$ of dust particles impacting on the surface of Ganymede is shown for two values of the ejecta size distribution power law exponent q. Table 6 shows the corresponding minimum and maximum values of flux on the surface of Ganymede.

Changing the exponent of the ejecta size distribution has little effect on the minimum and maximum values of the cumulative number flux. This is explained by the fact, that the chosen minimum size s_0 for our plots is the same as the sensitivity threshold s_{calib} of the Galileo DDS, to which the JMEM model is calibrated. Due to the choice of calibration, the cumulative flux is always dominated by grains of 0.3μm in size, regardless of the choice of the exponent q. For a larger cut-off size of $s_0 = 5\mu$m or more, the effect of the slope of the power law of ejecta size distribution would be more noticeable.

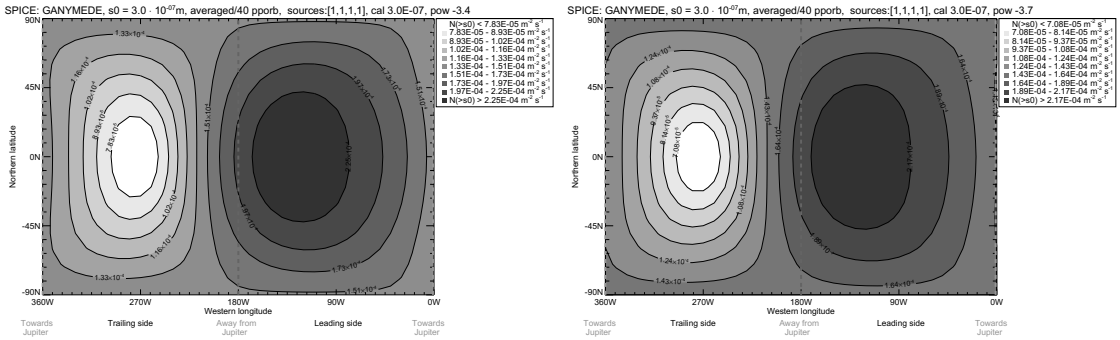

Figure 27: Comparison between power law exponents $q = 3.4$ (left) and $q = 3.7$ (right) for cumulative dust flux $N(> s_0)$ on the surface of Ganymede.

Exponent q	$q = 3.4$	$q = 3.7$
$N_{\min}$	$6.86 \cdot 10^{-5} \frac{1}{\mathrm{m^2 s}}$	$6.15 \cdot 10^{-5} \frac{1}{\mathrm{m^2 s}}$
$N_{\max}$	$2.57 \cdot 10^{-4} \frac{1}{\mathrm{m^2 s}}$	$2.49 \cdot 10^{-4} \frac{1}{\mathrm{m^2 s}}$

Table 6: Minimum and maximum values of cumulative dust number flux $N(> s_0)$ for two values of exponent q, impacting on the surface of Ganymede (see figure 27).

Employing a broken power law for the ejecta size distribution, with a knee around 100 microns, has a negligible effect on the number fluxes of micron-sized particles on the surface of the moons. For grains larger than 100μm, a mild effect is expected, which we have not evaluated quantitatively in this thesis.

In figure 28, the cumulative number flux $N(> s_0)$ of dust particles impacting on the surface of Ganymede is shown for two possible calibrations of the JMEM model based on in situ measurements of the Galileo DDS. Two values of detection threshold $s_{\mathrm{calib}} = 0.3\mu$m and $s_{\mathrm{calib}} = 0.6\mu$m are compared in the contour plots, and the corresponding minimum and maximum values of flux on the surface of Ganymede are gathered to table 7.

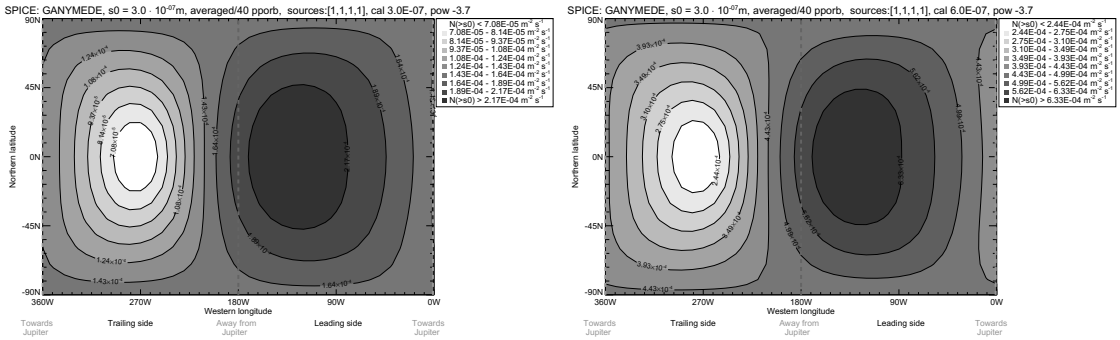

Figure 28: Effect of DDS calibration $s_{\mathrm{calib}} = 0.3\mu$m (left) and $s_{\mathrm{calib}} = 0.6\mu$m (right), for cumulative dust flux $N(> s_0)$ on the surface of Ganymede.

DDS calibration	0.3μm	0.6μm
N_{min}	$6.15 \cdot 10^{-5} \frac{1}{\mathrm{m^2 s}}$	$2.17 \cdot 10^{-4} \frac{1}{\mathrm{m^2 s}}$
N_{max}	$2.49 \cdot 10^{-4} \frac{1}{\mathrm{m^2 s}}$	$7.13 \cdot 10^{-4} \frac{1}{\mathrm{m^2 s}}$

Table 7: Minimum and maximum values of cumulative dust number flux $N(> s_0)$ for two modes of DDS calibration, impacting on the surface of Ganymede (see figure 28).

The calibration of the JMEM model by in situ measurements of the Galileo DDS has a noticeable effect on the flux received on the surface of the moons. However, the sensitivity threshold used in our plots should be the more plausible choice from the two possible options [52].

4.3.6 Comparison of total fluxes per second on the surface of the Galilean moons

In addition to comparing the minimum and maximum values of cumulative flux per second and square meter on the surface of the Galilean moons (see sections 4.3.2-4.3.5), the total flux per second on the surface of the moons J_{tot} can be estimated as well. By using the values of the surface areas $dA(k_\phi, k_\theta)$ of the individual elements

$$dA(k_\phi, k_\theta) = R^2_{\mathrm{moon}} \sin(k_\theta) d\theta d\phi \,, \tag{36}$$

of the surface area grid of the target moon in question (see figure 3), and the values of cumulative flux $N(k_\phi, k_\theta)$ per second and per square meter stored individually for each of these surface elements, we get an estimate of the number flux per second $J(k_\phi, k_\theta)$ on each element by simply multiplying the surface area of the element with the cumulative number flux value of that element

$$J(k_\phi, k_\theta) = dA(k_\phi, k_\theta) N(k_\phi, k_\theta) \,. \tag{37}$$

An estimate for the total number flux per second J_{tot} on the surface of the moon is then achieved by taking a sum of these individual elements

$$J_{\text{tot}} = \Sigma J(k_\phi, k_\theta)\,. \tag{38}$$

The values of total number flux per second J_{tot} on the surface of each target moon, for an array of minimum sizes s_0, are included in table 8.

Target:	Io	Europa	Ganymede	Callisto
$J_{\text{tot}}(> 0.3\mu\text{m})$	$2.08 \cdot 10^{10} \frac{1}{s}$	$3.32 \cdot 10^{10} \frac{1}{s}$	$1.37 \cdot 10^{10} \frac{1}{s}$	$3.40 \cdot 10^{9} \frac{1}{s}$
$J_{\text{tot}}(> 0.6\mu\text{m})$	$4.49 \cdot 10^{9} \frac{1}{s}$	$3.81 \cdot 10^{9} \frac{1}{s}$	$3.32 \cdot 10^{9} \frac{1}{s}$	$5.41 \cdot 10^{8} \frac{1}{s}$
$J_{\text{tot}}(> 1\mu\text{m})$	$4.09 \cdot 10^{9} \frac{1}{s}$	$3.80 \cdot 10^{9} \frac{1}{s}$	$9.84 \cdot 10^{8} \frac{1}{s}$	$1.99 \cdot 10^{8} \frac{1}{s}$
$J_{\text{tot}}(> 5\mu\text{m})$	$8.15 \cdot 10^{7} \frac{1}{s}$	$9.83 \cdot 10^{7} \frac{1}{s}$	$3.28 \cdot 10^{7} \frac{1}{s}$	$6.85 \cdot 10^{6} \frac{1}{s}$

Table 8: An estimate of the total number flux of dust per second on the surface of the Galilean moons, for an array of minimum sizes s_0 (other JMEM parameters are set to their default values of $s_{\text{calib}} = 0.3\mu\text{m}$, continuous power law of ejecta distribution with $q = 3.7$).

From table 8 it is seen, that the total cumulative number flux per second on the Galilean moons is roughly of the same order of magnitude for the three innermost moons Io, Europa and Ganymede. The largest total flux per second, around 2-3 times larger than on Io and Ganymede, is seen on Europa. The flux on Callisto is an order of magnitude smaller than the flux on Europa.

5 Discussion and conclusions

The aim of this thesis was to evaluate the fluxes of dust in the Jupiter system on the surfaces of each of the Galilean moons, using the results on the dust environment of the moons from the Jovian Meteoroid Environment Model (JMEM). The impact rates of dust are of principle interest, because this influx of material can noticeably change the physical properties and composition of the surface of the moons. An overview of the scientific background for the structure and composition of the Galilean moons, and for the jovian dust environment in general, was provided for the reader in section 2.

The set goal for this thesis was achieved by using the software Interactive Data Language (IDL) to create a program that employs functions from JMEM and constructs the fluxes on a given surface element of a moon. The cumulative number flux of dust grains larger than a given radius s_0 was then evaluated for the moons for a variety of different choices of parameters in the model. Contour

plots showing the cumulative flux on the surfaces of the moons were produced to visualize the effect of these parameters for the dust configuration (see section 4.3).

Through these contour plots, leading-trailing asymmetries for the flux of dust impacting on the surface of the moons were identified and interpreted in light of a simple analytical model that was developed for comparison for the results from JMEM (see section 3). In this analytical model, a synthetic dust ring of particles with identical semimajor axis a_{dust}, but distributed values of eccentricity ϵ, was created to study three prototype situations: flux on a moon located radially inside the dust ring, radially outside the dust ring, and at the center of the ring. For a moon located interior to the dust source, the maximum value of flux is expected on its trailing side, and for a moon located exterior to the source, a maximum flux value on its leading side is anticipated. On a moon located inside the dust ring, the majority of the flux is predicted to hit the surface of the moon from its jovian and anti-jovian directions.

From the comparison it was found that the deviation from the predictions of the analytical Keplerian model is significant for sub-micrometer grains. This can be attributed to the strong effect of (mainly) non-gravitational perturbation forces that act on the smaller grain sizes in the Jupiter system. The general behaviour of larger grains of $> 1\mu$m or $> 5\mu$m in radius, however, was well within our theoretical expectations. Another reason for the detected differences between the two models is, that in JMEM all the orbital elements are distributed quantities, not just the eccentricity of the dust orbit. Additionally, in JMEM the dust originated from all four Galilean moons is included, unlike in the analytical model where the semimajor axis of dust was kept constant, which corresponds to having a singular source moon for the dust material.

The amplitude of the leading-trailing asymmetries of the dust number flux onto the surface of the moons turned out to be moderate, amounting typically to a factor of 2-5 only (see table 1). For Europa the difference between the maximum and minimum values of flux on its surface is the smallest from the four moons ($N_{\mathrm{max,Europa}} \approx 1.6 N_{\mathrm{min,Europa}}$). For Ganymede ($N_{\mathrm{max,Ganymede}} \approx 4.1 N_{\mathrm{min,Ganymede}}$) and Io ($N_{\mathrm{max,Io}} \approx 4.9 N_{\mathrm{min,Io}}$) the amplitude was much more noticeable than for Europa. The outermost moon Callisto had the largest difference between its minimum and maximum values of flux ($N_{\mathrm{max,Callisto}} \approx 5.5 N_{\mathrm{min,Callisto}}$). From these results we see that the Galilean moons receive a significant dust flux all over their surfaces. This may be due to the fact that the spread of eccentricities ϵ and inclinations i of dust orbits present in the Jupiter system is large, and the random nature of the dust grain i and ϵ has a significant effect on the relative velocity of the dust grains impacting on the surface, in addition to the effect of the orbital velocity of the moons. Nevertheless, we conclude that the non-isotropy of the dust infall over the surface should lead to a marked difference of the distribution of

external material on the surfaces of the Galilean moons.

The total flux of particles per second J_{tot} on the surface of the Galilean moons is between $3.4 \cdot 10^{9} \frac{1}{\text{s}} - 3.3 \cdot 10^{10} \frac{1}{\text{s}}$ for grains larger than $s_0 = 0.3\mu$m. For a larger $s_0 = 5\mu$m cut-off radius, the total fluxes on the moons are around 2-3 orders of magnitude lower, approximately between $6.9 \cdot 10^{6} \frac{1}{\text{s}} - 9.8 \cdot 10^{7} \frac{1}{\text{s}}$ (see table 8). The largest total flux per second for all cut-off sizes is seen on Europa, which is not surprising, since the moon is located roughly at the distance from Jupiter where the density of the Galilean ring is highest. On the innermost moon Io the total flux is somewhat lower, but still fairly close to the value on Europa, around $J_{\text{tot,Io}} = 0.63 J_{\text{tot,Europa}}$. The flux on Ganymede, which is located exterior to Europa's orbit, is also roughly of the same order of magnitude ($J_{\text{tot,Ganymede}} = 0.41 J_{\text{tot,Europa}}$). On the outermost Galilean moon Callisto, the total flux per second is an order of magnitude lower than the flux on Europa ($J_{\text{tot,Callisto}} = 0.10 J_{\text{tot,Europa}}$). Overall, the total flux on the surface of the four moons seems to follow a similar dependence on their radial distance from Jupiter as the radial dust density in JMEM model does.

For future work related to the topic of this thesis, utilizing the new enhanced version of JMEM (currently in development by Liu [2]), with dust configuration results evaluated in a frame that keeps a fixed orientation with respect to the Sun, would be interesting. Using such configurations will allow the exploration of the azimuthal asymmetries present in the jovian dust environment, and their possible effect on the fluxes of dust on the Galilean moons.

Other promising topics for the continuation of the work outlined in this thesis would be to estimate the total mass fluxes and energy deposition of the dust fluxes on the surface of the moons. Estimating the mass flux, and from therein the total volume of the flux of dust exchanged between the Galilean moons, would in turn lead to an estimate of the typical layer depths of dust on the moons. Constraining this value would help in providing important information about the layer depths of exogenic material on different locations on the surface of the moons. This information would be valuable for future mission landings that plan to collect samples from the surface of the Galilean moons.

References

[1] H. Krüger, M. Horányi, A. V. Krivov, and Graps A. L. Jovian dust: streams, clouds and rings. *Cambridge University Press*, pages 219–240, 2004.

[2] Xiaodong Liu, Manuel Sachse, Frank Spahn, and Jürgen Schmidt. Dynamics and distribution of Jovian dust ejected from the Galilean satellites. *Journal of Geophysical Research (Planets)*, 121:1141–1173, July 2016.

[3] Kai-Uwe Thiessenhusen, Harald Krüger, Frank Spahn, and Eberhard Grün. Dust grains around jupiter—the observations of the galileo dust detector. *Icarus*, 144(1):89 – 98, 2000.

[4] Harald Krüger, Alexander V. Krivov, Douglas P. Hamilton, and Eberhard Grün. Detection of an impact-generated dust cloud around Ganymede. *Nature*, 399:558–560, June 1999.

[5] H. Krüger, P. Geissler, M. Horányi, A. L. Graps, S. Kempf, R. Srama, G. Moragas-Klostermeyer, R. Moissl, T. V. Johnson, and E. Grün. Jovian dust streams: A monitor of Io's volcanic plume activity. *Geophysical Research Letters*, 30(21), 2003.

[6] Olivier Witasse. JUICE (Jupiter Icy Moon Explorer): A European mission to explore the emergence of habitable worlds around gas giants. In *EPSC-DPS Joint Meeting 2019*, volume 2019, pages EPSC–DPS2019–400, Sep 2019.

[7] J. J. Plaut, S. Barabash, L. Bruzzone, M. Dougherty, C. Erd, L. Fletcher, R. Gladstone, O. Grasset, L. Gurvits, P. Hartogh, H. Hussmann, L. Iess, R. Jaumann, Y. Langevin, P. Palumbo, G. Piccioni, D. Titov, and J. E. Wahlund. Jupiter Icy Moons Explorer (JUICE): Science Objectives, Mission and Instruments. In *Lunar and Planetary Science Conference*, Lunar and Planetary Science Conference, page 2717, Mar 2014.

[8] X. Liu, M. Sachse, and J. Schmidt. Technical Description of the Meteoroid Model., Technical Description (TD) in the project Jovian Meteoroid Environment Model (JMEM) of the European Space Agency (ESA), contract No.4000107249/12/NL/AF. 2015.

[9] J. Schmidt. Jovian Meteoroid Environment Model: Installation of the User Interface and Manual., User Manual (UM) of the User Interface in the project Jovian Meteoroid Environment Model (JMEM) of the European Space Agency (ESA), contract No.4000107249/12/NL/AF. 2015.

[10] B. A. Smith, L. A. Soderblom, T. V. Johnson, A. P. Ingersoll, S. A. Collins, E. M. Shoemaker, G. E. Hunt, H. Masursky, M. H. Carr, M. E. Davies, A. F. Cook II, J. Boyce, G. E. Danielson, T. Owen, C. Sagan, R. F. Beebe, J. Veverka, R. G. Strom, J. F. McCauley, D. Morrison, G. A. Briggs, and V. E. Suomi. The jupiter system through the eyes of voyager 1. *Science*, 204(4396), 1979.

[11] H. Krüger, A. L. Graps, D. P. Hamilton, A. Flandes, R. J. Forsyth, M. Horányi, and E. Grün. Ulysses jovian latitude scan of high-velocity dust streams originating from the jovian system. *Planetary and Space Science*, 54(9-10), 2006.

[12] Eberhard Gruen, Hugo Fechtig, Martha S. Hanner, Jochen Kissel, Bertil-Anders Lindblad, Dietmar Linkert, Dieter Maas, Gregor E. Morfill, and Herbert A. Zook. The Galileo Dust Detector. *ssr*, 60(1-4):317–340, May 1992.

[13] Candice J. Hansen, Scott J. Bolton, Dennis L. Matson, Linda J. Spilker, and Jean-Pierre Lebreton. The Cassini-Huygens flyby of Jupiter. *Icarus*, 172(1):1–8, Nov 2004.

[14] I. de Pater, M. R. Showalter, J. A. Burns, P. D. Nicholson, M. C. Liu, D. P. Hamilton, and J. R. Graham. Keck Infrared Observations of Jupiter's Ring System near Earth's 1997 Ring Plane Crossing. *Icarus*, 138, 1999.

[15] M. H. Wong, I. de Pater, M. R. Showalter, H. G. Roe, B. Macintosh, and G. Verbanac. Ground-based near infrared spectroscopy of Jupiter's ring and moons. *Icarus*, 185, 2006.

[16] I. de Pater, M. R. Showalter, and B. Macintosh. Keck observations of the 2002 2003 jovian ring plane crossing. *Icarus*, 195, 2008.

[17] J. A. Burns, M. R. Showalter, and G. E. Morfill. The ethereal rings of Jupiter and Saturn. In R. Greenberg and A. Brahic, editors, *IAU Colloq. 75: Planetary Rings*, pages 200–272, January 1984.

[18] M. R. Showalter, A. F. Cheng, H. A. Weaver, S. A. Stern, J. R. Spencer, H. B. Throop, E. M. Birath, D. Rose, and J. M. Moore. Clump Detections and Limits on Moons in Jupiter's Ring System. *Science*, 318:232–, October 2007.

[19] H. B. Throop, R. A. West, J. A. Burns, M. R. Showalter, P. D. Nicholson, and C. C. Porco. The jovian rings: New results derived from Cassini, Galileo, Voyager, and Earth-based observations. *Icarus*, 172(1 SPEC.ISS.), 2004.

[20] S. M. Brooks, L. W. Esposito, M. R. Showalter, and H. B. Throop. The size distribution of Jupiter's main ring from Galileo imaging and spectroscopy. *Icarus*, 170(1), 2004.

[21] E. Grün, G. E. Morfill, and D. A. Mendis. Dust-magnetosphere interactions. In *IAU Colloq. 75: Planetary Rings*, pages 275–332, 1984.

[22] M. R. Showalter, J. A. Burns, J. N. Cuzzi, and J. B. Pollack. Jupiter's ring system: New results on structure and particle properties. *Icarus*, 69(3):458–498, March 1987.

[23] M. E. Ockert-Bell, J. A. Burns, I. J. Daubar, P. C. Thomas, J. Veverka, M. J. S. Belton, and K. P. Klaasen. The Structure of Jupiter's Ring System as Revealed by the Galileo Imaging Experiment. *Icarus*, 138(2), 1999.

[24] J. A. Burns, D. P. Simonelli, M. R. Showalter, D. P. Hamilton, C. D. Porco, H. Throop, and L. W. Esposito. Jupiter's ring-moon system. *Cambridge University Press*, pages 241–262, 2004.

[25] M. Horányi and A. Juhász. Plasma conditions and the structure of the jovian ring. *Journal of Geophysical Research (Space Physics)*, 115, 2010.

[26] J. A. Burns, M. R. Showalter, D. P. Hamilton, P. D. Nicholson, I. De Pater, M. E. Ockert-Bell, and P. C. Thomas. The formation of Jupiter's faint rings. *Science*, 284(5417), 1999.

[27] M. R. Showalter, I. de Pater, G. Verbanac, D. P. Hamilton, and J. A. Burns. Properties and dynamics of Jupiter's gossamer rings from Galileo, Voyager, Hubble and Keck images. *Icarus*, 195(1), 2008.

[28] Harald Krüger, Douglas P. Hamilton, Richard Moissl, and Eberhard Grün. Galileo in-situ dust measurements in Jupiter's gossamer rings. *Icarus*, 203, 2009.

[29] H. Krüger, E. Grün, M. Landgraf, M. Baguhl, S. Dermott, H. Fechtig, B. A. Gustafson, D. P. Hamilton, M. S. Hanner, M. Horányi, J. Kissel, B. A. Lindblad, D. Linkert, G. Linkert, I. Mann, J. A. M. McDonnell, G. E. Morfill, C. Polanskey, G. Schwehm, R. Srama, and H. A. Zook. Three years of Ulysses dust data: 1993-1995. *Planss*, 47, 1999.

[30] E. Grün, M. Baguhl, N. Divine, H. Fechtig, D. P. Hamilton, M. S. Hanner, J. Kissel, B.-A. Lindblad, D. Linkert, G. Linkert, I. Mann, J. A. M. McDonnell, G. E. Morfill, C. Polanskey, R. Riemann, G. Schwehm, N. Siddique, P. Staubach, and H. A. Zook. Two years of Ulysses dust data. *Planss*, 43, 1995.

[31] H. Krüger, E. Grün, M. Landgraf, S. Dermott, H. Fechtig, B. A. Gustafson, D. P. Hamilton, M. S. Hanner, M. Horányi, J. Kissel, B. A. Lindblad, D. Linkert, G. Linkert, I. Mann, J. A. M. McDonnell, G. E. Morfill, C. Polanskey, G. Schwehm, R. Srama, and H. A. Zook. Four years of Ulysses dust data: 1996-1999. *Planss*, 49, 2001.

[32] H. Krüger, N. Altobelli, B. Anweiler, S. F. Dermott, V. Dikarev, A. L. Graps, E. Grün, B. A. Gustafson, D. P. Hamilton, M. S. Hanner, M. Horányi, J. Kissel, M. Landgraf, B. A. Lindblad, D. Linkert, G. Linkert, I. Mann, J. A. M. McDonnell, G. E. Morfill, C. Polanskey, G. Schwehm, R. Srama, and H. A. Zook. Five years of Ulysses dust data: 2000 2004. *Planss*, 54, 2006.

[33] H. Krüger, V. Dikarev, B. Anweiler, S. F. Dermott, A. L. Graps, E. Grün, B. A. Gustafson, D. P. Hamilton, M. S. Hanner, M. Horányi, J. Kissel, D. Linkert, G. Linkert, I. Mann, J. A. M. McDonnell, G. E. Morfill, C. Polanskey, G. Schwehm, and R. Srama. Three years of Ulysses dust data: 2005 to 2007. *planss*, 58, 2010.

[34] H. Krüger, E. Grün, A. Graps, D. Bindschadler, S. Dermott, H. Fechtig, B. A. Gustafson, D. P. Hamilton, M. S. Hanner, M. Horányi, J. Kissel, B. A. Lindblad, D. Linkert, G. Linkert, I. Mann, J. A. M. McDonnell, G. E. Morfill, C. Polanskey, G. Schwehm, R. Srama, and H. A. Zook. One year of Galileo dust data from the Jovian system: 1996. *planss*, 49, 2001.

[35] H. Krüger, D. Bindschadler, S. F. Dermott, A. L. Graps, E. Grün, B. A. Gustafson, D. P. Hamilton, M. S. Hanner, M. Horányi, J. Kissel, B. A. Lindblad, D. Linkert, G. Linkert, I. Mann, J. A. M. McDonnell, R. Moissl, G. E. Morfill, C. Polanskey, G. Schwehm, R. Srama, and H. A. Zook. Galileo dust data from the jovian system: 1997 1999. *planss*, 54, 2006.

[36] H. Krüger, D. Bindschadler, S. F. Dermott, A. L. Graps, E. Grün, B. A. Gustafson, D. P. Hamilton, M. S. Hanner, M. Horányi, J. Kissel, D. Linkert, G. Linkert, I. Mann, J. A. M. McDonnell, R. Moissl, G. E. Morfill, C. Polanskey, M. Roy, G. Schwehm, and R. Srama. Galileo dust data from the jovian system: 2000 to 2003. *planss*, 58, 2010.

[37] A. Flandes. Dust escape from Io. *grl*, 31, 2004.

[38] M. Horanyi, G. Morfill, and E. Gruen. The dusty ballerina skirt of Jupiter. *Journal of Geophysical Research*, 98(A12):21245–21252, December 1993.

[39] Alexander V. Krivov, Ingo Wardinski, Frank Spahn, Harald Krüger, and Eberhard Grün. Dust on the Outskirts of the Jovian System. *Icarus*, 157:436–455, June 2002.

[40] T. Denk, S. Mottola, F. Tosi, W. F. Bottke, and D. P. Hamilton. *The Irregular Satellites of Saturn*, page 409. 2018.

[41] David Jewitt and Nader Haghighipour. Irregular Satellites of the Planets: Products of Capture in the Early Solar System. *Annual Reviews of Astronomy and Astrophysics*, 45(1):261–295, September 2007.

[42] W. F. Bottke, D. Nesvorný, D. Vokrouhlický, and A. Morbidelli. The Irregular Satellites: The Most Collisionally Evolved Populations in the Solar System. *aj*, 139, 2010.

[43] P. D. Nicholson, M. Cuk, S. S. Sheppard, D. Nesvorny, and T. V. Johnson. *Irregular Satellites of the Giant Planets*, page 411. 2008.

[44] H. Krüger, A. V. Krivov, and E. Grün. A dust cloud of Ganymede maintained by hypervelocity impacts of interplanetary micrometeoroids. *Planetary and Space Science*, 48:1457–1471, December 2000.

[45] Harald Krüger, Alexander V. Krivov, Miodrag Sremčević, and Eberhard Grün. Impact-generated dust clouds surrounding the Galilean moons. *Icarus*, 164:170–187, July 2003.

[46] M. Sremčević, A. V. Krivov, H. Krüger, and F. Spahn. Impact-generated dust clouds around planetary satellites: Model versus galileo data. *Planetary and Space Science*, 53(6), 2005.

[47] Alexander V. Krivov, Miodrag Sremčević, Frank Spahn, Valeri V. Dikarev, and Konstantin V. Kholshevnikov. Impact-generated dust clouds around planetary satellites: spherically symmetric case. *Planetary and Space Science*, 51:251–269, March 2003.

[48] M. Sremčević, A. V. Krivov, F. Spahn, and H. Krueger. Asymmetric model of impact-generated dust clouds around Galilean moons. In *EGS - AGU - EUG Joint Assembly, Abstracts from the meeting held in Nice, France, 6 - 11 April 2003, abstract id.10424*, April 2003.

[49] Miodrag Sremčević, Alexander V. Krivov, and Frank Spahn. Impact-generated dust clouds around planetary satellites: asymmetry effects. *Planetary and Space Science*, 51(7-8):455–471, June 2003.

[50] D. H. Humes, J. M. Alvarez, R. L. O'Neal, and W. H. Kinard. The interplanetary and near-Jupiter meteoroid environments. *Journal of Geophysical Research*, 79(25):3677, January 1974.

[51] D. B. Zeehandelaar and D. P. Hamilton. A Local Source for the Pioneer 10 and 11 Circumjovian Dust Detections. In H. Krueger and A. Graps, editors, *Dust in Planetary Systems*, volume 643 of *ESA Special Publication*, pages 103–106, January 2007.

[52] A. V. Krivov, H. Krüger, E. Grün, K. U Thiessenhusen, and D. P. Hamilton. A tenuous dust ring of jupiter formed by escaping ejecta from the galilean satellites. *Journal of Geophysical Research E: Planets*, 107(1), 2002.

[53] Manuel Sachse. A planetary dust ring generated by impact-ejection from the Galilean satellites. *Icarus*, 303:166–180, March 2018.

[54] F. Sohl, T. Spohn, D. Breuer, and K. Nagel. Implications from Galileo Observations on the Interior Structure and Chemistry of the Galilean Satellites. *Icarus*, 157(1):104–119, May 2002.

[55] J. D. Anderson, W. L. Sjogren, and G. Schubert. Galileo Gravity Results and the Internal Structure of Io. *Science*, 272(5262):709–712, May 1996.

[56] J. D. Anderson, E. L. Lau, W. L. Sjogren, G. Schubert, and W. B. Moore. Gravitational constraints on the internal structure of Ganymede. *Nature*, 384(6609):541–543, Dec 1996.

[57] J. D. Anderson, E. L. Lau, W. L. Sjogren, G. Schubert, and W. B. Moore. Europa's differentiated internal structure: Inferences from two Galileo encounters. *Science*, 276:1236–1239, May 1997.

[58] J. D. Anderson, E. L. Lau, W. L. Sjogren, G. Schubert, and W. B. Moore. Gravitational evidence for an undifferentiated Callisto. *Nature*, 387(6630):264–266, May 1997.

[59] William B. McKinnon. NOTE: Mystery of Callisto: Is It Undifferentiated? *Icarus*, 130(2):540–543, December 1997.

[60] J. D. Anderson, G. Schubert, R. A. Jacobson, E. L. Lau, W. B. Moore, and W. L. Sjogren. Europa's Differentiated Internal Structure: Inferences from Four Galileo Encounters. *Science*, 281:2019, Sep 1998.

[61] J. D. Anderson, R. A. Jacobson, E. L. Lau, W. B. Moore, O. Olsen, G. Schubert, P. C. Thomas, and Galileo Gravity Science Team. Shape, Mean Radius, Gravity Field and Interior Structure of Ganymede. In *AAS/Division for Planetary Sciences Meeting Abstracts #33*, volume 33 of *AAS/Division for Planetary Sciences Meeting Abstracts*, page 35.09, November 2001.

[62] J. D. Anderson, R. A. Jacobson, T. P. McElrath, W. B. Moore, G. Schubert, and P. C. Thomas. Shape, Mean Radius, Gravity Field, and Interior Structure of Callisto. *Icarus*, 153(1):157–161, Sep 2001.

[63] M. G. Kivelson, K. K. Khurana, R. J. Walker, C. T. Russell, J. A. Linker, D. J. Southwood, and C. Polanskey. A Magnetic Signature at Io: Initial Report from the Galileo Magnetometer. *Science*, 273(5273):337–340, Jul 1996.

[64] M. G. Kivelson, K. K. Khurana, C. T. Russell, R. J. Walker, J. Warnecke, F. V. Coroniti, C. Polanskey, D. J. Southwood, and G. Schubert. Discovery of Ganymede's magnetic field by the Galileo spacecraft. *Nature*, 384(6609):537–541, December 1996.

[65] D. A. Gurnett, W. S. Kurth, A. Roux, S. J. Bolton, and C. F. Kennel. Evidence for a magnetosphere at Ganymede from plasma-wave observations by the Galileo spacecraft. *Nature*, 384(6609):535–537, December 1996.

[66] M. G. Kivelson, K. K. Khurana, F. V. Coroniti, S. Joy, C. T. Russell, R. J. Walker, J. Warnecke, L. Bennett, and C. Polanskey. The magnetic field and magnetosphere of Ganymede. *Geophysical Research Letters*, 24(17):2155–2158, Sep 1997.

[67] M. G. Kivelson, K. K. Khurana, C. T. Russell, R. J. Walker, P. J. Coleman, F. V. Coroniti, J. Green, S. Joy, R. L. McPherron, C. Polanskey, D. J. Southwood, L. Bennett, J. Warnecke, and D. E. Huddleston. Galileo at Jupiter: changing states of the magnetosphere and first looks at IO and ganymede. *Advances in Space Research*, 20(2):193–204, Jan 1997.

[68] M. G. Kivelson, J. Warnecke, L. Bennett, S. Joy, K. K. Khurana, J. A. Linker, C. T. Russell, R. J. Walker, and C. Polanskey. Ganymede's magnetosphere: Magnetometer overview. *Journal of Geophysical Research*, 103(E9):19963–19972, Sep 1998.

[69] Margaret G. Kivelson, Krishan K. Khurana, Christopher T. Russell, Martin Volwerk, Raymond J. Walker, and Christophe Zimmer. Galileo Magnetometer Measurements: A Stronger Case for a Subsurface Ocean at Europa. *Science*, 289(5483):1340–1343, Aug 2000.

[70] A. S. McEwen, L. P. Keszthelyi, L. Rosaly, P. M. Schenk, and J. R. Spencer. *The Lithosphere and Surface of Io*, page 281. 2007.

[71] Cynthia Baya Phillips. *Voyager and Galileo SSI views of volcanic resurfacing on Io and the search for geologic activity on Europa*. PhD thesis, THE UNIVERSITY OF ARIZONA, September 2000.

[72] G. Schubert, J. D. Anderson, T. Spohn, and W. B. McKinnon. *Interior Composition, Structure and Dynamics of the Galilean Satellites*, page 281. 2007.

[73] S. J. Peale, P. Cassen, and R. T. Reynolds. Melting of Io by Tidal Dissipation. *Science*, 203(4383):892–894, March 1979.

[74] S. J. Peale. Origin and Evolution of the Natural Satellites. *Annual Reviews of Astronomy and Astrophysics*, 37:533–602, January 1999.

[75] Oleg L. Kuskov and Victor A. Kronrod. Core Sizes and Internal Structure of Earth's and Jupiter's Satellites. *Icarus*, 151(2):204–227, June 2001.

[76] A. S. McEwen, L. Keszthelyi, J. R. Spencer, G. Schubert, D. L. Matson, R. Lopes-Gautier, K. P. Klaasen, T. V. Johnson, J. W. Head, P. Geissler, S. Fagents, A. G. Davies, M. H. Carr, H. H. Breneman, and M. J. S. Belton. High-Temperature Silicate Volcanism on Jupiter's Moon Io. *Science*, 281:87, July 1998.

[77] Alfred S. McEwen, Laszlo Keszthelyi, Paul Geissler, Damon P. Simonelli, Michael H. Carr, Torrence V. Johnson, Kenneth P. Klaasen, H. Herbert Breneman, Todd J. Jones, James M. Kaufman, Kari P. Magee, David A. Senske, Michael J. S. Belton, and Gerald Schubert. Active Volcanism on Io as Seen by Galileo SSI. *Icarus*, 135:181–219, September 1998.

[78] Oleg L. Kuskov and Victor A. Kronrod. Resemblance and difference between the constitution of the Moon and Io. *Planetary and Space Science*, 48(7-8):717–726, June 2000.

[79] John D. Anderson, Robert A. Jacobson, Eunice L. Lau, William B. Moore, and Gerald Schubert. Io's gravity field and interior structure. *Journal of Geophysical Research*, 106(E12):32963–32970, December 2001.

[80] M. G. Kivelson, K. K. Khurana, C. T. Russell, and R. J. Walker. Magnetic Signature of a Polar Pass Over Io. In *AGU Fall Meeting Abstracts*, volume 2001, pages P11A–01, December 2001.

[81] K. K. Khurana, . M. G. Kivelson, C. T. Russell, R. J. Walker, and S. Joy. Io's Magnetic Field. In *EGS General Assembly Conference Abstracts*, EGS General Assembly Conference Abstracts, page 5119, January 2002.

[82] Rosaly M. C. Lopes and David A. Williams. Io after Galileo. *Reports on Progress in Physics*, 68(2):303–340, February 2005.

[83] R. Greeley, C. F. Chyba, J. W. Head III, T. B. McCord, W. B. McKinnon, R. T. Pappalardo, and P. H. Figueredo. *Geology of Europa*, page 281. 2007.

[84] K. K. Khurana, M. G. Kivelson, D. J. Stevenson, G. Schubert, C. T. Russell, R. J. Walker, and C. Polanskey. Induced magnetic fields as evidence for subsurface oceans in Europa and Callisto. *Nature*, 395(6704):777–780, October 1998.

[85] M. G. Kivelson, K. K. Khurana, D. J. Stevenson, L. Bennett, S. Joy, C. T. Russell, R. J. Walker, C. Zimmer, and C. Polanskey. Europa and Callisto: Induced or intrinsic fields in a periodically varying plasma environment. *Journal of Geophysical Research*, 104(A3):4609–4626, March 1999.

[86] Christophe Zimmer, Krishan K. Khurana, and Margaret G. Kivelson. Subsurface Oceans on Europa and Callisto: Constraints from Galileo Magnetometer Observations. *Icarus*, 147(2):329–347, October 2000.

[87] R. T. Pappalardo, G. C. Collins, J. W. Head III, P. Helfenstein, T. B. McCord, J. M. Moore, L. M. Prockter, P. M. Schenk, and J. R. Spencer. *Geology of Ganymede*, page 281. 2007.

[88] W. B. McKinnon and S. Desai. Internal Structures of the Galilean Satellites: What Can We Really Tell? In Stephen Mackwell and Eileen Stansbery, editors, *Lunar and Planetary Science Conference*, Lunar and Planetary Science Conference, page 2104, March 2003.

[89] Gerald Schubert, Keke Zhang, Margaret G. Kivelson, and John D. Anderson. The magnetic field and internal structure of Ganymede. *Nature*, 384(6609):544–545, December 1996.

[90] M. G. Kivelson, K. K. Khurana, and M. Volwerk. The Permanent and Inductive Magnetic Moments of Ganymede. *Icarus*, 157(2):507–522, June 2002.

[91] K. K. Khurana, M. G. Kivelson, C. T. Russell, R. J. Walker, and D. J. Southwood. Absence of an internal magnetic field at Callisto. *Nature*, 387(6630):262–264, May 1997.

[92] European Space Agency (ESA). JUpiter ICy moons Explorer Mission Site. `https://sci.esa.int/web/juice/home`. Accessed: 2020-02-20.

[93] The JUICE Science Study Team. JUICE assessment study report (Yellow Book), ESA/SRE(2011)18. `https://sci.esa.int/documents/33960/35865/1567258126055-JUICE_Yellow_Book_Issue1.pdf`, 2012.

[94] Rosario Lorente, Nicolas Altobelli, Claire Vallat, Claudio Muñoz, Rafael Andrés, Marc Costa, Olivier Witasse, and Christian Erd. JUICE: a European mission to Jupiter and its icy moons. In *EGU General Assembly Conference Abstracts*, EGU General Assembly Conference Abstracts, page 15281, April 2018.

[95] National Aeronautics and Space Administration (NASA). Europa Clipper Mission Site. `https://www.jpl.nasa.gov/missions/europa-clipper/`. Accessed: 2020-02-20.

[96] Cynthia B. Phillips and Robert T. Pappalardo. Europa Clipper Mission Concept: Exploring Jupiter's Ocean Moon. *EOS Transactions*, 95(20):165–167, May 2014.

[97] David Senske, Robert Pappalardo, Haje Korth, Diana Blaney, Don Blankenship, Phil Christensen, Kurt Retherford, Elizabeth Turtle, and Kathleen Craft. Science of the Europa Clipper Mission: Comprehensive Remote Sensing to Investigate the Ice Shell. In *EPSC-DPS Joint Meeting 2019*, volume 2019, pages EPSC–DPS2019–731, Sep 2019.

[98] Sarah A. Fagents, Ronald Greeley, Robert J. Sullivan, Robert T. Pappalardo, Louise M. Prockter, and Galileo SSI Team. Cryomagmatic Mechanisms for the Formation of Rhadamanthys Linea, Triple Band Margins, and Other Low-Albedo Features on Europa. *Icarus*, 144(1):54–88, Mar 2000.

[99] Sarah A. Fagents. Considerations for effusive cryovolcanism on Europa: The post-Galileo perspective. *Journal of Geophysical Research (Planets)*, 108(E12):5139, Dec 2003.

[100] Lynnae C. Quick, Olivier S. Barnouin, Louise M. Prockter, and G. Wesley Patterson. Constraints on the detection of cryovolcanic plumes on Europa. *Planetary andSpaceScience*, 86:1–9, Sep 2013.

[101] Lorenz Roth, Joachim Saur, Kurt D. Retherford, Darrell F. Strobel, Paul D. Feldman, Melissa A. McGrath, and Francis Nimmo. Transient Water Vapor at Europa's South Pole. *Science*, 343(6167):171–174, Jan 2014.

[102] W. B. Sparks, K. P. Hand, M. A. McGrath, E. Bergeron, M. Cracraft, and S. E. Deustua. Probing for Evidence of Plumes on Europa with HST/STIS. *The Astrophysical Journal*, 829(2):121, Oct 2016.

[103] W. B. Sparks, B. E. Schmidt, M. A. McGrath, K. P. Hand , J. R. Spencer, M. Cracraft, and S. E Deustua. Active Cryovolcanism on Europa? *The Astrophysical Journal Letters*, 839(2):L18, Apr 2017.

[104] Lynnae C. Quick, Lori S. Glaze, and Stephen M. Baloga. Cryovolcanic emplacement of domes on Europa. *Icarus*, 284:477–488, Mar 2017.

[105] B. S. Southworth, S. Kempf, and J. Schmidt. Modeling Europa's dust plumes. *Geophysical Research Letters*, 42(24):10,541–10,548, December 2015.

[106] J. Schmidt. Jovian Meteoroid Environment Model JMEM: Executive summary. 2017.

[107] M. Horányi, J. R. Szalay, S. Kempf, J. Schmidt, E. Grün, R. Srama, and Z. Sternovsky. A permanent, asymmetric dust cloud around the Moon. *Nature*, 522(7556):324–326, June 2015.

[108] J. Schmidt, X. Liu, M. Sachse, and F. Spahn. Jovian Meteoroid Environment Model JMEM: Final Report. 2017.

[109] H. McNamara, J. Jones, B. Kauffman, R. Suggs, W. Cooke, and S. Smith. Meteoroid Engineering Model (MEM): A Meteoroid Model For The Inner Solar System. *Earth Moon and Planets*, 95(1-4):123–139, December 2004.

[110] V. Dikarev, E. Grün, J. Baggaley, D. Galligan, M. Landgraf, and R. Jehn. The new ESA meteoroid model. *Advances in Space Research*, 35(7):1282–1289, January 2005.